nature communications

Article

https://doi.org/10.1038/s41467-025-66436-x

# Norepinephrine-mediated arousal fluctuations drive inverted U-shaped functional connectivity dynamics

Received: 20 June 2025

Accepted: 7 November 2025

Published online: 13 December 2025

Check for updates

Chuanjun Tong[1,4] ✉, Weishuai Li[1,2,4], Yijuan Zou[3,4], Ying Xia[1], Mengchao Pei[1], Kaiwei Zhang[1], Yichao Luo[1] & Zhifeng Liang[1] ✉

Arousal states dynamically shape brain function and behavioral performance, as posited by the Yerkes-Dodson law. Yet, functional network substrates underlying this inverted U-shaped pattern remain unknown. Here, by integrating functional magnetic resonance imaging (fMRI) with simultaneous electroencephalography (EEG) across humans and awake mice, we found arousal modulated inverted U-shaped global functional connectivity (FC) dynamics, peaking at middle arousal level. Such inverted U-shaped FC exhibited significant correlation with arousal modulated behavioral performance, recapitulating the Yerkes-Dodson framework at the functional network level. Further combining invasive multimodal neural recording and manipulations of locus coeruleus-norepinephrine (LC-NE) neurons with awake mouse EEG-fMRI, we revealed the causal contribution of LC-NE system to arousal modulated FC dynamics, in which the inverted U-shaped pattern was dependent on the baseline arousal level. To summarize, we uncovered the functional network basis of the Yerkes-Dodson law, which was causally driven by the NE-mediated arousal fluctuations.

Arousal states affect how we process information and respond to our environment with profound and complex regulatory effects on global brain dynamics[1]. The Yerkes-Dodson law[2] posits that human moderate arousal optimizes decision-making and sensory integration, whereas both hypo- or hyper-arousal impair behavioral performance. Rodent studies also revealed behavioral performance peaked at moderate arousal level and degraded at extreme arousal levels in various behavioral paradigms, such as the detection task[3,4]. This cross-species conserved behavioral principle underscored arousal's dual role as both facilitator and disruptor of adaptive functions. However, the underlying functional network substrates are yet to be clearly undefined. Crucially, whether this behavioral principle arises from arousal-dependent reconfiguration of whole-brain functional networks, and whether such dynamics persist across both resting and task-evoked states, remain unclear.

Extensive studies have examined the relationship between arousal and functional networks, highlighting the arousal-dependent functional network dynamics[5–12]. However, contradictory results of arousal effects on functional networks dynamics have been reported. Human functional magnetic resonance imaging (fMRI) studies revealed increased whole-brain functional connectivity (FC) with decreased arousal level from eye-open to eye-closed state[5–8]. In contrast, human fMRI studies with simultaneous electroencephalography (EEG) recording showed strengthened whole-brain FC with increased arousal from non-rapid eye movement (NREM) sleep to wakefulness[9–11]. Nevertheless, our awake marmoset fMRI work identified inverted U-shaped FC gradient dynamics with increasing arousal, indexed by both pupil size and fMRI-based index[12]. This discrepancy likely stemmed from heterogeneous arousal quantification methods, including pupillometry[5–8], EEG spectra[9–11], and fMRI-based arousal index[12]. Such

[1]Institute of Neuroscience, International Center for Primate Brain Research, Center for Excellence in Brain Science and Intelligence Technology, State Key Laboratory of Genetic Evolution & Animal Models, Chinese Academy of Sciences, Shanghai, China. [2]University of Chinese Academy of Sciences, Beijing, China. [3]Changping Laboratory, Beijing, China. [4]These authors contributed equally: Chuanjun Tong, Weishuai Li, Yijuan Zou.
✉e-mail: tongcj@ion.ac.cn; zliang@ion.ac.cn

diverse quantification of arousal levels renders above results not quantitatively comparable. Furthermore, for vast majority of fMRI studies lacking arousal monitoring, unaccounted arousal fluctuations may confound interpretations of FC alterations[13], therefore demanding further exploration and clarification of arousal effects on FC dynamics.

One of potential regulators for mediating the arousal effects on FC dynamics is the locus coeruleus-norepinephrine (LC-NE) system[14], which is the predominant noradrenergic source in mammalian brain[15–18]. LC-NE neurons exhibit both tonic and phasic firing patterns that modulate attention and arousal. Several studies have proposed that variations along these modes can contribute to an inverted U-shaped relation between noradrenergic drive and performance[14,15,19]. However, the extent, mechanisms, and generalizability of this relationship remain debated and likely depend on task context, receptor engagement, and brain state. Moreover, rodent fMRI combining precise neuromodulation techniques, such as optogenetics and chemogenetics, provides a platform to probe the causal relationship between LC-NE system and FC dynamics. After chemogenetic activation of LC-NE neurons in anesthetized mice[20,21], significant increase of FC was observed. Nevertheless, how LC-NE modulated FC increases observed under low-arousal anesthesia mapped onto the inverted U-shaped relationship between arousal and behavior in the awake state remains unclear.

Therefore, it is crucial to establish the causal relationship among LC-NE system, arousal, and whole-brain functional networks. In this study, combining awake mouse and human fMRI in resting and task-evoked states with simultaneous EEG, i.e., gold standard to quantify arousal level, we revealed arousal modulated inverted U-shaped global FC across both species and behavioral states, exhibiting significant correlation with behavioral performance with arousal fluctuations. When causally up and downregulating LC-NE neuronal activity using optogenetics and chemogenetics fMRI, we demonstrated LC-NE system causally drove arousal-dependent FC dynamics, and such NE effect on global FC dynamics was dependent on the baseline arousal level and the direction of arousal-FC change. In summary, by integrating cross-species EEG-fMRI with causal LC-NE regulations, we demonstrated NE mediated arousal fluctuations drive inverted U-shaped functional connectivity dynamics. Our work outlined a cross-species, baseline-dependent inverted U-shaped relationship between arousal and global FC, with LC-NE activity serving as a causal driver of FC dynamics.

## Results

### Arousal modulated inverted U-shaped whole-brain FC in human resting state and task-evoked state

To dissect the role of arousal fluctuations in shaping whole-brain functional network dynamics and behavioral performance, we first utilized the openly accessible human detection task fMRI dataset[22] (Fig. 1A). Participants were engaged in a spatial detection task to quickly determine the location of high-salience image[22]. Pupil size was simultaneously acquired and used as a behavioral arousal index (Fig. 1A). After our highly optimized fMRI denoising preprocessing[12,23,24] (Supplementary Fig. 1) and regressing out the task block structure from BOLD signals, we employed the dynamic conditional correlation (DCC) approach[25] to estimate whole-brain dynamic FC. Then, whole-brain dynamic FC matrices were binned into 8 intervals according to the pupil-based arousal index, ranging from low to high arousal levels (Supplementary Fig. 2). As expected, the reaction time during behavioral tasks peaked at the middle arousal level (Fig. 1B), whereas a weak but still significant inverted U-shaped trend of performance accuracy along with increasing pupil size. Importantly, arousal fluctuations showed an inverted U-shaped relationship with global FC changes (Fig. 1C). Moreover, such arousal-modulated inverted U-shaped FC dynamics were significantly correlated with participants' behavioral performance (Fig. 1D, E), suggesting the arousal-modulated inverted U-shaped whole-brain FC could serve as an attractive indicator for explaining variations in task-related behavioral performance.

To explore whether the inverted U-shaped relationship also existed in resting state fMRI, we utilized the simultaneous EEG-fMRI dataset of human natural sleep[26] with behavioral monitoring through eye-tracking and button-pressing (Fig. 1F). Continuous EEG-fMRI recording revealed substantial arousal fluctuations spanning awake and NREM sleep states, accompanied by notable fMRI signal dynamics (Supplementary Fig. 2). To quantify the arousal level, the ratio of the power in the alpha band (7–13 Hz) to the theta band (3–7 Hz) was defined as the human EEG-based arousal index[27], achieving a refined second-by-second arousal estimation. Considering the potential systematic hemodynamic differences in the sleep-wake cycle[28–30], only EEG-fMRI data in awake state was included in analysis. Dynamic FC matrices were binned into 30 intervals based on the EEG-based arousal index, ranging from low (drowsy) to high (alert) arousal levels (Supplementary Fig. 2). The matrices within each bin were averaged to determine global FC (Fig. 1G). Along with increasing arousal level, the monotonic elevation of pupil size and button-pressing rate, i.e., external behavioral proxy of arousal, demonstrated the accuracy and validity of our EEG-based arousal index (Fig. 1G, H). Notably, the global FC exhibited an inverted U-shaped relationship with arousal (Fig. 1G, H, Averaged global FC: Low v.s. Middle, $p = 0.0014$; Middle v.s. High, $p = 0.0130$; Low v.s. High, $p = 0.6601$; Pupil size: Low v.s. Middle, $p = 0.0042$; Middle v.s. High, $p = 0.0102$; Low v.s. High, $p = 0.0024$; Button-press rate: Low v.s. Middle, $p = 0.0220$; Middle v.s. High, $p = 0.2864$; Low v.s. High, $p = 0.0427$). Such inverted U-shaped arousal-FC relationship, i.e., increasing from low to middle arousal level but decreasing at higher arousal level (Fig. 1G, H), resembled that during human detection task (Fig. 1C). Region-wise comparison showed predominately global, yet regionally differentiated, spatial patterns (Fig. 1I), which was in line with the inverted U-shaped pattern for global FC (Fig. 1G).

Of note, head motion could potentially bias estimates of arousal-FC relationship if not treated carefully. After applying our preprocessing pipeline, i.e., "6 rp + 6 Δrp + M PCs" regression, we observed the correlation between arousal indices and frame-wise displacement (FD) of preprocessed fMRI signals became statistically non-significant (Supplementary Fig. 3), underscoring the effectiveness of our nuisance signal regression-based denoising strategy in mitigating motion-related confounds. To further verify the inverted U-shaped pattern was not affected by preprocessing strategy and the methodology of dynamic FC estimation, we compared the dynamic FC using different combinations of nuisance regressors, e.g., global signal (Supplementary Fig. 4A–C), and the sliding window approach with different window sizes (Supplementary Fig. 4D–F). Importantly, the inverted U-shaped pattern was consistent across all control analyses (Supplementary Fig. 4G), demonstrating minimal computational bias in our primary results.

### Cross-species and cross-modal conserved arousal modulated inverted U-shaped pattern in mice

Next, we utilized our previous mouse sleep fMRI dataset[24], which captured a broad spectrum of arousal fluctuations across awake, NREM, and rapid eye movement (REM) sleep states (Fig. 2A) using intracranial EEG (iEEG) -fMRI. Considering the relatively low signal-to-noise ratio (SNR) of raw fMRI images from mouse iEEG-fMRI dataset, we firstly conducted a seed-based connectivity analysis revealing canonical mouse functional networks (Supplementary Fig. 5), demonstrating the data were of sufficient quality to capture resting-state network organization. Then, similar to the above human analysis, only data in awake state was included. The inverse of the power in 2–10 Hz band was defined as mouse iEEG-based arousal index[1]

https://doi.org/10.1038/s41467-025-66436-x

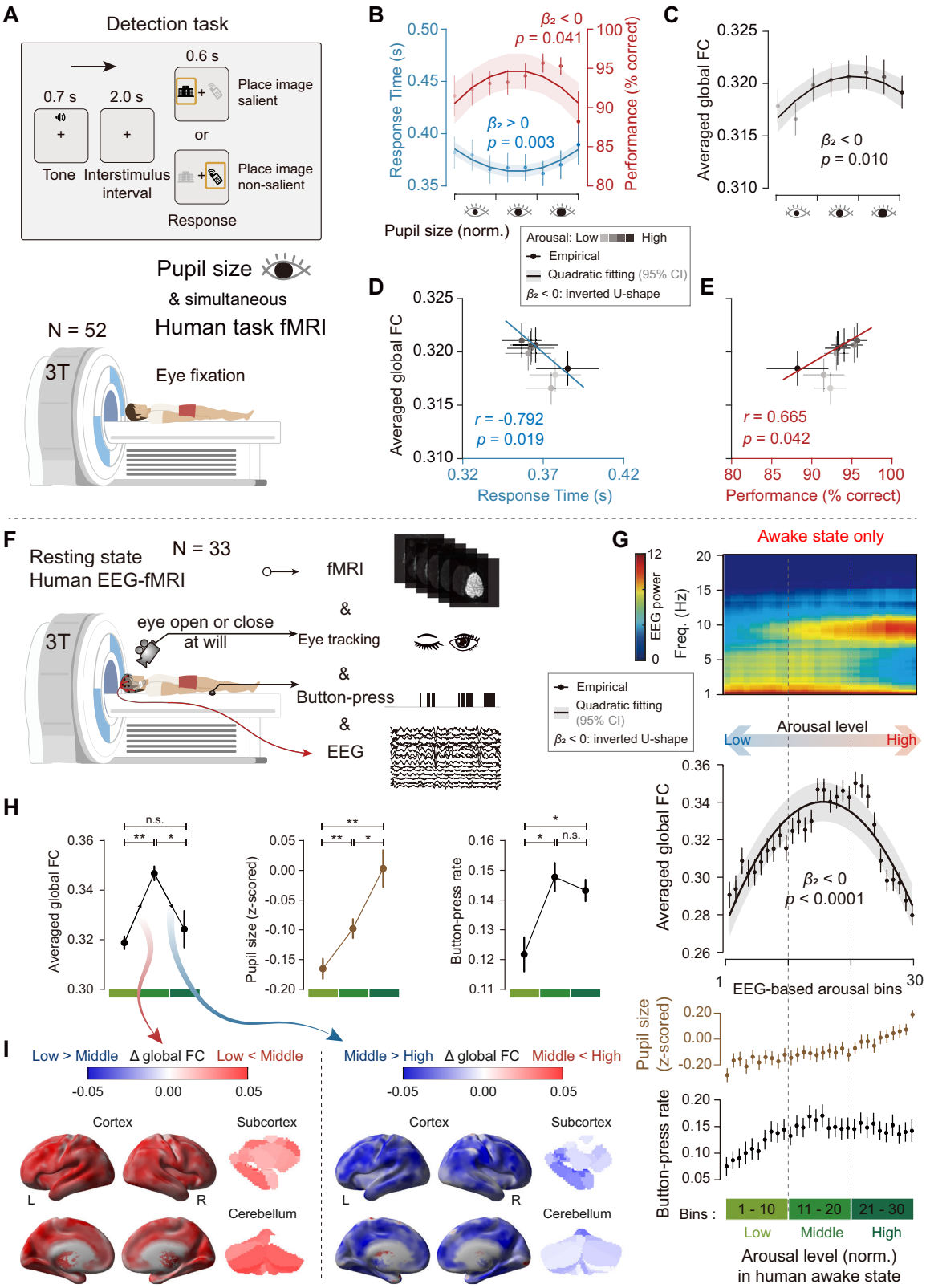


(Fig. 2A). We found a consistent arousal modulated inverted U-shaped pattern of whole-brain FC in awake mice (Fig. 2B, C, Averaged global FC: Low v.s. Middle, $p = 0.0032$; Middle v.s. High, $p = 0.0268$; Low v.s. High, $p = 0.4875$). Similarly, these arousal effects on FC dynamics were predominately global, yet regionally differentiated (Fig. 2D and Supplementary Fig. 6), highlighting a cross-species conserved pattern between humans and mice.

Moreover, we conducted a series of parallel analyses to demonstrate whether the inverted arousal-FC relationship was contingent on a single, narrow-band definition. Accordingly, we systematically varied EEG frequency band edges, i.e., off by one, two, or more Hz, and re-derived the arousal index for humans (Supplementary Fig. 7A–C) and mice (Supplementary Fig. 7D, E). Across all sets, the inverted U-shaped global FC-arousal relationship persisted with consistent negative

https://doi.org/10.1038/s41467-025-66436-x

**Fig. 1 | Inverted U-shaped relationship between arousal and whole-brain FC in human detection task and resting states. A** Human detection task fMRI with simultaneous pupil size recording. **B** U-shaped response time and inverted U-shaped correction rate with the increasing arousal level as indexed by the pupil size (8 bins). Behavioral performance was fitted to a quadratic curve $y = \beta_2 x^2 + \beta_1 x + \beta_0$, and the $\beta_2 < 0$ represented an inverted U-shaped profile. **C** Arousal modulated inverted U-shaped whole-brain FC changes in human detection task. The task block structure was regressed out from the BOLD signals before the dynamic FC estimation. **D**, **E** Significant correlation between behavioral performance and arousal sorted dynamic FC. Each dot represented an individual arousal bin as in (**B**, **C**). Red or blue line, the best linear fitting. Solid line (or shade) in (**B**, **C**), the best fitting of quadratic curve (or the 95% prediction interval). Sample size in (**B**–**E**): $n = 52$ runs for each bin. Error bar in (**B**–**E**), the standard error of the mean (SEM). **F** Human EEG-fMRI with simultaneous eye-tracking and button-pressing recording. **G** Inverted U-shaped relationship between whole-brain global dynamic FC and arousal level in awake state. The EEG power spectrum, global FC, pupil size, and button-press rate were sorted and averaged along with the increasing arousal level as indexed by EEG (30 bins). Black solid line (or shade), the best fitting of quadratic curve (or the 95% prediction interval). Sample size $n = 158$ runs for each bin. Error bar, the SEM. **H** Quantitative evaluations of arousal aligned dynamic FC, pupil size, and button-press rate changes. Thirty arousal bins in (**G**) were further trisected into three bins, i.e., low, middle, and high. Sample size $n = 10$ bins for each arousal level. Error bar, the SEM. Statistical significance was determined by the paired $t$-test (two tails). n.s. no significance; *, $p < 0.05$; **, $p < 0.01$. **I** Arousal modulated whole-brain spatial pattern of global FC changes. Upper, global FC difference of middle minus low arousal level; lower, that of high minus middle arousal level. Source data are provided as a Source Data file.

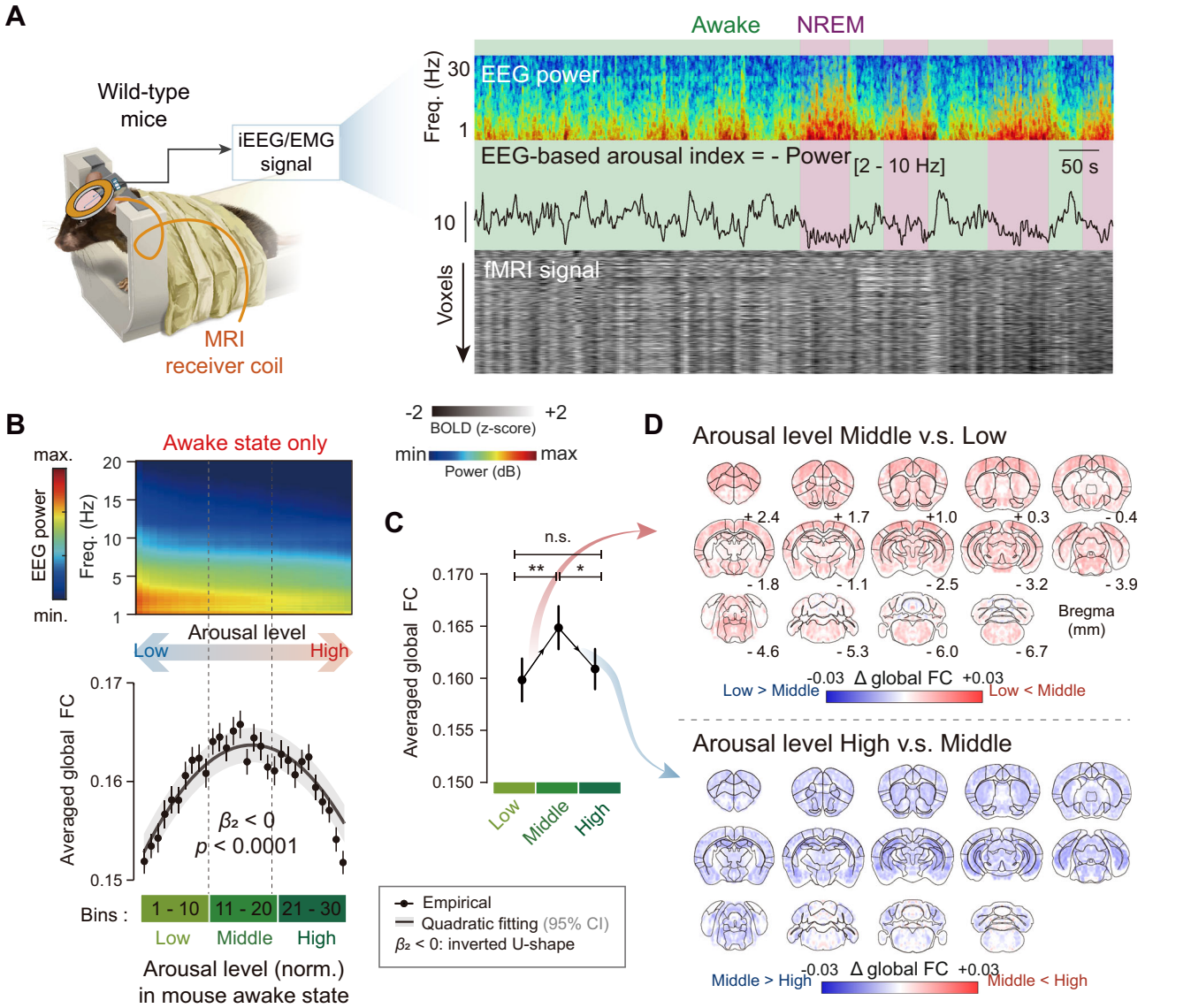


**Fig. 2 | Simultaneous mouse iEEG-fMRI revealed consistent inverted U-shaped relationship between arousal and whole-brain FC as in human. A** Simultaneous iEEG-fMRI in non-anesthetized mice ($n = 46$ sessions) captured a broad spectrum of arousal dynamics across awake and non-rapid eye movement (NREM) sleep states. EMG electromyography. **B** Arousal modulated inverted U-shaped whole-brain FC dynamics in awake mice. The dynamic FCs were fitted to a quadratic curve $y = \beta_2 x^2 + \beta_1 x + \beta_0$, and the $\beta_2 < 0$ represented an inverted U-shaped profile. Black solid line (or shade), the best fitting of quadratic curve (or the 95% prediction interval). Sample size $n = 46$ runs for each bin. Error bar, the standard error of the mean (SEM). **C** Quantitative evaluations of arousal aligned FC dynamics. Sample size $n = 10$ bins for each arousal level. Error bar, the SEM. Statistical significance was determined by the paired $t$-test (two tails). n.s. no significance; *, $p < 0.05$, **, $p < 0.01$. **D** Arousal modulated whole-brain spatial pattern of global FC changes in mice. Source data are provided as a Source Data file.

quadratic patterns, indicating our result was not driven by a narrow, idiosyncratic choice of (i)EEG frequency bands.

To further confirm the neural basis of such inverted U-shaped pattern, wide-field calcium imaging data in mice[31] was utilized to simultaneously record neural activities, EEG and pupil size (Supplementary Fig. 8A, B) across natural wake and sleep states. Using data from awake state, the global calcium-based FC exhibited an inverted U-shaped relationship with arousal (Supplementary Fig. 8C, D, Averaged global calcium-based FC: Low v.s. Middle, $p = 0.0226$; Middle v.s. High, $p < 0.0001$; Low v.s. High, $p = 0.5559$; Pupil size: Low v.s. Middle, $p = 0.0012$; Middle v.s. High, $p < 0.0001$; Low v.s. High, $p < 0.0001$), supporting above fMRI results in mice and humans (Figs. 1 and 2). And the spatial pattern of arousal modulated FC dynamics was also predominantly global and regionally differentiated (Supplementary Fig. 8E). Importantly, such calcium-based FC exhibited significant spatial correlation with fMRI-based FC in awake mice (Supplementary Fig. 8F), further demonstrating the underlying neural basis of arousal modulated inverted U-shaped whole-brain FC.

Meanwhile, based on the wide-field calcium imaging results in mice, we first identified the arousal bin with the highest calcium-based global FC (Supplementary Fig. 9A–D) to explore the tonic-like arousal effect on global FC dynamics. We found highest global FC in DMN-like regions occurred at lower arousal level, whereas highest global FC in primary sensorimotor areas occurred at higher arousal level. However, such arousal binning emphasized the absolute tonic-like arousal level and did not distinguish the phase of arousal cycle, i.e., rise, peak, and fall. Then, we applied phase-aligned analysis for EEG-based arousal index and calcium-based FC. Briefly, we segmented phasic-like arousal cycles in awake mice, temporally aligned the EEG-based arousal index to yield a canonical rise-peak-fall trajectory, and averaged the corresponding global calcium-based FC within phase-aligned arousal (Supplementary Fig. 9E, F). Spatially, highest FC in primary sensorimotor areas occurred in the peak phase of arousal (highest arousal), whereas highest FC in DMN-like and visual regions occurred in the falling phase (decreasing arousal) (Supplementary Fig. 9C, F). Moreover, we did not observe apparent regions showing highest FC in the rise phase of the arousal cycle. Thus, such phase-dependent phenomenon, i.e., all highest FC occurred in the peak and falling phase of the arousal cycle, indicated that increasing arousal preceded global FC elevation within an arousal cycle, rather than FC changes preceding arousal fluctuations.

## Contribution of LC-NE system to arousal-modulated inverted U-shaped whole-brain FC

Although above (i)EEG-fMRI results showed globally distributed spatial patterns between dynamic FC and arousal, the regional heterogeneity still existed. Therefore, we set out to explore whether a cluster of core regions or connections predominantly contributed to the inverted U-shaped pattern (Fig. 3A). Based on EEG-fMRI results from humans (Fig. 1) and mice (Fig. 2), we calculated the correlation between each dynamic FC edge and the global FC, and defined such correlation coefficient as the sensitivity to arousal fluctuations (Fig. 3B). For each edge, higher correlation coefficient indicated higher sensitivity to arousal. The sensitivity of each node (brain region) was calculated as averaged sensitivity with other nodes (Fig. 3C). In human fMRI, we found the top 10% nodes with highest sensitivity primarily located in sensorimotor, dorsal attention and salience networks (Fig. 3D). Importantly, arousal also highly modulated the FC of dorsal raphe (DR), LC and parabrachial nucleus (PB) in the brainstem (Fig. 3D), which are known key regions in arousal modulation[32]. To quantitatively evaluate whether these nodes with higher sensitivity contributed more to the inverted U-shaped pattern, we permuted the dynamic FC edges across arousal bins and tested whether the inverted U-shape persisted or not. After orderly permuting brain regions from the highest to lowest sensitivity, the arousal modulated inverted U-shaped architecture collapsed at a faster rate than random permutations without considering their sensitivity (Fig. 3E).

Similar results were observed in mice (Fig. 3F), in which the most sensitive nodes located in visual, motor, salience[33], and brainstem areas (Fig. 3G). Specifically, these arousal-modulated regions in mouse brainstem showed large overlap with the ascending neuromodulatory system[32], including LC, DR, substantia nigra (SNr), ventral tegmental area (VTA), hypothalamus ventral premammillary nucleus (PMv), and basal forebrain (BF) (Fig. 3G). Permutation analysis in mice (Fig. 3H) resembled those conducted in humans, again highlighting the key contribution of these highest sensitive nodes. Notably, the spatial profile of arousal-modulated nodes correlated strongly with axonal projections of neuromodulatory cell types (Fig. 3I). Among these, the anatomical projection from LC-NE neurons exhibited the highest spatial correlation compared to other types (Fig. 3I, LC-NE: $r = 0.42$, $p = 0.0003$; BF-Ach: $r = 0.29$, $p = 0.0261$; DR-5HT: $r = 0.18$, $p = 0.0602$; VTA-DA: $r = 0.08$, $p = 0.1415$; PMv-HA: $r = 0.30$, $p = 0.0118$), indicating the LC-NE system may play a crucial role in the arousal-modulated whole-brain FC dynamics.

To experimentally explore the contribution of LC-NE system, simultaneous fiber photometry recording of GCaMP6s-based calcium signal of LC-NE neurons and extracellular NE signals in prefrontal cortex (PFC) and primary somatosensory cortex (SSp-bfd) using the NE biosensor[34,35] $GRAB_{NE\text{-}2h}$ (Supplementary Fig. 10) was further incorporated into our sleep iEEG-fMRI setup[24] using DBH-Cre mice (Fig. 4A). Continuous recordings covering multiple sleep-awake cycles (Fig. 4B) revealed a notable infra-slow arousal fluctuation accompanied by cortical NE dynamics. As expected, peaks of LC-NE neuronal activity lead to the sequential increase of cortical extracellular NE concentrations (~2.5 s delay) and iEEG-based arousal index (~5.2 s delay) (Fig. 4C), suggesting the LC-NE activity preceded the arousal change. Combing the phase-aligned calcium-FC findings (Supplementary Fig. 9), we could extend this temporal sequence from LC-NE to arousal, then to global FC dynamics. Again, the whole-brain FC exhibited an inverted U-shaped profile with increasing NE concentration and LC-NE neuronal activity from low to high arousal level (Fig. 4D, E, Averaged global FC: Low v.s. Middle, $p = 0.0349$; Middle v.s. High, $p = 0.0484$; Low v.s. High, $p = 0.8456$; LC-NE neuron $Ca^{2+}$: Low v.s. Middle, $p = 0.0447$; Middle v.s. High, $p = 0.2624$; Low v.s. High, $p = 0.0008$; NE sensor: Low v.s. Middle, $p = 0.4054$; Middle v.s. High, $p = 0.1823$; Low v.s. High, $p = 0.0082$). In conclusion, these findings demonstrated that the NE-mediated arousal fluctuations exhibited an inverted U-shaped relationship with whole-brain FC (Fig. 4F).

## Casual contribution of LC-NE system to arousal-modulated whole-brain FC

The above results suggested a close relationship between NE and whole-brain FC dynamics. To further explore such relationship causally, we manipulated NE concentrations through up and down-regulations of LC-NE neuronal activity using optogenetics and chemogenetics fMRI in awake and anesthetized mice (Figs. 5–7).

First, stabilized step-function opsin (SSFO) hChR2(C128S D156A)-mCherry or mCherry-only virus was expressed in bilateral LC-NE neurons (Fig. 5A and Supplementary Fig. 11) served as SSFO or Sham group, respectively. Periodic blue and yellow light was delivered to bilateral LC for selectively activating or terminating such activation of NE neurons (Fig. 5B) during simultaneous recording of cortical NE concentration, iEEG, and fMRI signals in awake mice. SSFO-based activation of LC-NE neurons significantly elevated cortical NE concentration (Fig. 5C, SSFO v.s. Sham: $p = 0.0031$) and the iEEG-based arousal index (SSFO ON v.s. OFF: $p = 0.0231$, Sham ON v.s. OFF: $p = 0.5632$) from the middle to high arousal level with ~1 min delay (Fig. 5D and Supplementary Fig. 12), compared to the Sham group. Consistent with the right half of the inverted U-shape (from middle to high arousal level), we observed significant decreases of global FC after

https://doi.org/10.1038/s41467-025-66436-x

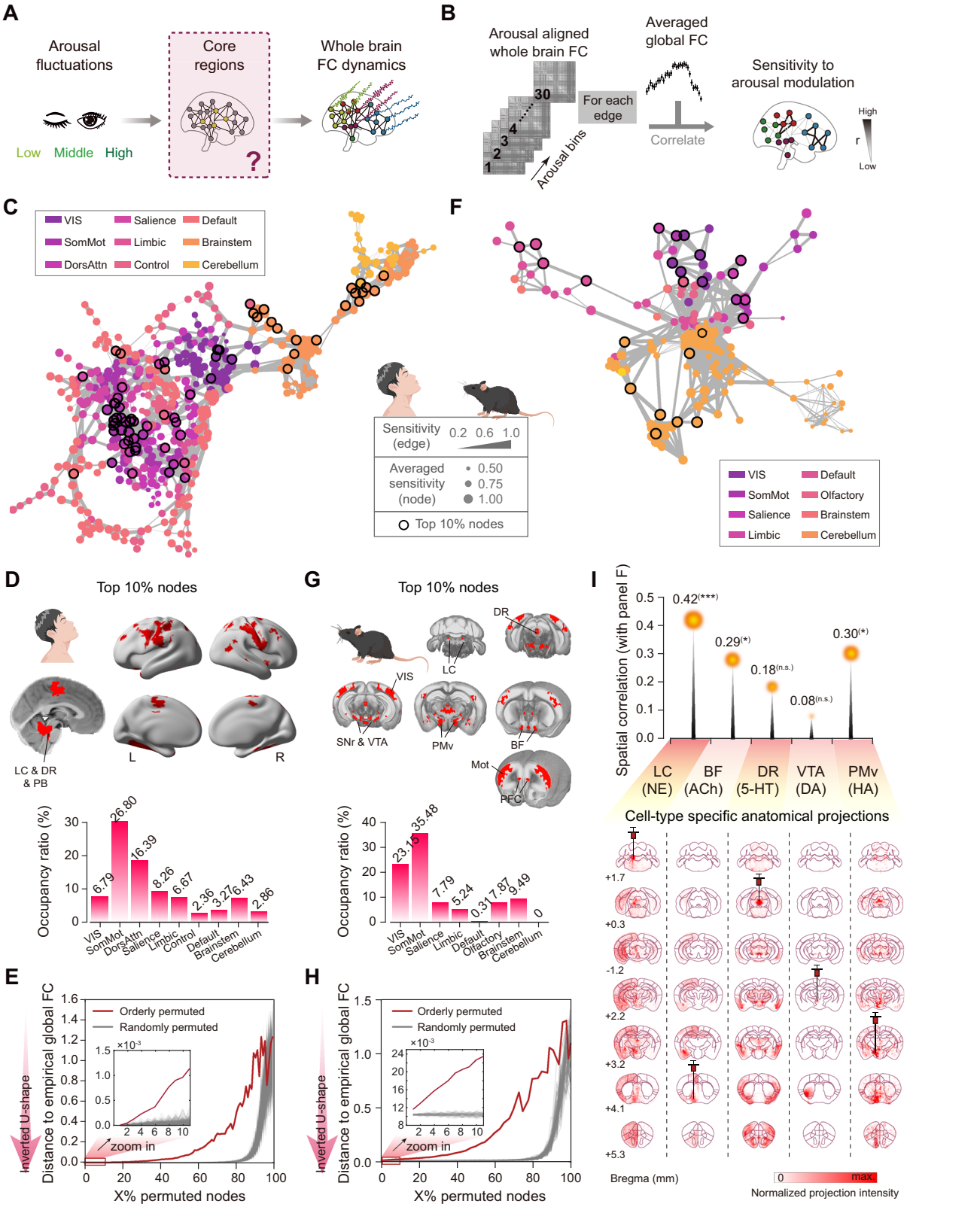


SSFO-based activation (Fig. 5E, F, SSFO v.s. Sham: $p = 0.0136$), demonstrating that increased NE led to higher arousal level with a corresponding decrease of whole-brain FC in awake mice (Fig. 5G).

Next, the inhibitory opsin stGtACR2-mCherry or mCherry-only was expressed in bilateral LC-NE neurons (Supplementary Fig. 11), respectively, with similar awake mouse multimodal fMRI setup (Fig. 6A, B) to the above SSFO experiment. stGtACR2-based inactivation of LC-NE neurons significantly decreased cortical NE concentration (Fig. 6C, stGtACR2 v.s. Sham: $p = 0.0362$) and the iEEG-based arousal index from the middle to low arousal level with ~2 min delay (Fig. 6D, stGtACR2 ON v.s. OFF: $p = 0.0026$, Sham ON v.s. OFF: $p = 0.5636$), compared to the Sham group. Consistent with the left half of the inverted U-shape (from middle to low arousal level), we observed significant decreases of global FC after stGtACR2-based

**Fig. 3 | LC-NE system contributed to the inverted U-shaped relationship between arousal and whole-brain FC. A** Hypothesis: A cluster of core regions bridge the arousal fluctuations and whole-brain FC dynamics. **B** Correlation between dynamic FC of each edge and the global one was defined as the sensitivity of arousal modulation. For each node, the sensitivity was calculated as the averaged sensitivity with other regions based on the corresponding brain parcellation. **C** Force-directed layout of the human arousal modulated sensitivity matrix. Line width represented the sensitivity of arousal modulation. Top 10% nodes with highest sensitivity were encircled in black. Cortical 7 functional network definition[64] was adopted from Schaefer et. al. **D** Spatial distribution of nodes with top 10% sensitivity in human. Occupancy ratio was defined as the ratio of the voxel number of top 10% nodes to the total voxel number in each functional network. VIS visual, SomMot sensorimotor, DorsAtten dorsal attention. DR dorsal raphe, PB parabrachial nucleus. **E** Faster collapse of arousal modulated inverted U-shaped pattern on whole-brain FC after the orderly permutation than random permutations ($n = 1000$ times). The permutation was conducted across arousal bins for each node. Lower distance indicated a more similar inverted U-shaped pattern. **F**–**H** As in (**C**–**E**), but for mice. For better visualization in (**F**), we used 296 ROIs from Allen Mouse Brain CCFv3 instead of 7657 parcels. Cortical functional network definition[33] was adopted from Zerbi et. al. SNr substantia nigra, VTA ventral tegmental area, BF basal forebrain, Mot motor, PFC prefrontal cortex. **I** Highest and significant spatial correlation between LC-NE anatomical projections and arousal-modulated spatial pattern (node). Anatomical projection maps were averaged cross-hemisphere for all cell types. Five cell-type specific anterograde axonal tracing were from the Allen Mouse Brain Connectivity Atlas. LC (NE), locus coeruleus (norepinephrine); BF (Ach), basal forebrain (acetylcholine); DR (5-HT), dorsal raphe (serotonin); VTA (DA), ventral tegmental area (dopamine); PMv (HA), hypothalamic ventral premammillary nucleus (histamine): experiment ID #511971714, #478491810, #114155190, #160539283, #157952068. Statistical significance of spatial correlation was determined using the spatial autocorrelation preserving shuffling (two-sided *t*-test, Details were shown in "Methods"). *, $p_{spin} < 0.05$; ***, $p_{spin} < 0.005$; n.s. no significance. Source data are provided as a Source Data file.

inactivation (Fig. 6E, F, stGtACR2 v.s. Sham: $p = 0.0188$), demonstrating that decreased NE led to lower arousal level with a corresponding decrease of whole-brain FC in awake mice (Fig. 6G).

Moreover, chemogenetic fMRI was also employed to activate LC-NE neurons in both awake and isoflurane anesthetized mice (Fig. 7A). The hM3Dq-mCherry or mCherry-only was expressed in bilateral LC-NE neurons (Supplementary Fig. 11) served as hM3Dq or Sham group, respectively. In awake mice, after the injection of clozapine, EEG-based arousal index significantly increased from a middle to high arousal level (Fig. 7B, hM3Dq pre v.s. post: $p = 0.0007$, Sham pre v.s. post: $p = 0.0031$), and whole-brain FC decreased compared to the Sham group (Fig. 7C–E, hM3Dq v.s. Sham, $p = 0.0126$). In isoflurane anesthetized mice, after the injection of clozapine, EEG-based arousal index also significantly increased, but from a low to middle arousal level (Fig. 7F, hM3Dq pre v.s. post: $p = 0.0003$, Sham pre v.s. post: $p = 0.0018$), accompanied by higher whole-brain FC compared to the Sham group[20] (Fig. 7G–I, hM3Dq v.s. Sham, $p = 0.0079$). Notably, the "middle" arousal under isoflurane anesthesia should not be assumed physiologically equivalent to the "middle" arousal in the awake state (Fig. 7). Isoflurane can shift neuromodulatory tone, vascular baselines, and neural excitability. Thus, in our study, the isoflurane condition was used to extend sampling of arousal spectrum into the qualitatively low arousal state. The integrated schematic diagram (Fig. 7) should be carefully viewed as a conceptual synthesis across arousal spectrum rather than a single continuous curve measured under one condition. Therefore, above two chemogenetics fMRI experiments demonstrated that the effect of NE upregulation on global FC dynamics is dependent on the baseline arousal level and the direction of arousal-FC change.

In conclusion, our findings demonstrate that arousal bidirectionally modulates whole-brain FC through an inverted U-shaped relationship, which is conserved in both humans and mice and can be driven by LC-NE system (Fig. 8). Global FC peaked at middle arousal level and decreased at the lower or higher arousal level. Such inverted U-shaped relationship from LC-NE activity to FC and behaviors highlighted the delicate balance required for optimal brain function with arousal. Understanding this nonlinearity provided critical insights into both normal cognition and neuropsychiatric disorders, paving the way for targeted interventions that restore equilibrium in the LC-NE system.

## Discussion

The LC-NE system is a key neuromodulator to influence arousal and behavioral performance, yet its causal role in linking arousal states to whole-brain functional connectivity (FC) remained unresolved. By integrating cross-species fMRI in humans and mice with multimodal neural recordings and manipulations, we revealed that LC-NE activity nonlinearly shaped whole-brain FC in an inverted U-shaped manner with arousal fluctuations. Critically, bidirectional optogenetic control of LC-NE neurons in awake mice causally demonstrated that both excessive and deficient NE levels reduced global FC strength, mirroring the decrease of global FC and behavioral performance in humans. Moreover, such inverted U-shaped pattern of NE-mediated FC dynamics was dependent on the baseline arousal level. In summary, these findings collectively demonstrated that NE-mediated arousal fluctuations drove inverted U-shaped FC dynamics, providing an avenue for explaining the arousal-modulated inverted U-shaped behavioral performance from the functional network view.

It has long been known that arousal levels have an inverted U-shaped relationship with behavioral performance, which is summarized by the Yerkes-Dodson law[2]. Previous studies focused on the regional neural activity[1,3] or neurotransmitter dynamics[36] to explore the underlying neural mechanisms. Our findings provided deeper understanding by revealing the functional network basis of behavioral inverted U-shape. Detection accuracy and global FC peaked at middle arousal level (Figs. 1 and 2) and middle NE concentrations (Fig. 4), which is consistent with the role of LC-NE system in promoting efficient decision-making and functional network reconfigurations[37,38]. From low to middle arousal level, the increase of global FC (Fig. 8) potentially reflected increased neuronal signal-to-noise ratios and enhanced information transformation modulated by increasing tonic NE release[19]. Beyond the middle arousal level, the decrease of global FC (Fig. 8) might be attribute to the desynchronization of slow fluctuations across brain regions meditated by phasic NE bursts[39]. Such arousal modulated inverted U-shaped global FC may explain why both hypo- and hyper-arousal degrade behavioral performance. Also, the overlap in high-sensitivity nodes modulated by arousal in humans and mice (Fig. 3D, G) revealed an evolutionarily conserved circuit architecture, including sensorimotor and salience networks, which are densely innervated by LC-NE axon projections (Fig. 3I). Therefore, the LC-NE system causally mediated arousal fluctuations and inverted U-shaped whole-brain FC dynamics, potentially reflecting the functional network basis of behavioral variability.

Notably, the inverted U-shape should not be assumed to generalize to deep anesthesia or to REM sleep. Our arousal proxies and mechanistic interpretation were for natural wakefulness only, where pupil, electrophysiological low frequency fluctuations, and LC-NE dynamics remain coupled[1,40,41] and neurovascular baselines are relatively stable. Therefore, we explicitly excluded NREM and REM sleep epochs for the FC analyses in human and mouse multimodal neuroimaging datasets (Figs. 1–6). The anesthetized chemogenetics-fMRI result (Fig. 7) was included only to sample the low-arousal state under light isoflurane. Therefore, we did not aim to generalize our conclusions to other conditions, such as deep anesthesia and (N)REM sleep states. In summary, we emphasized that the inverted U-shaped arousal-FC relationship we reported held for natural wakefulness and for light, low-arousal anesthesia or light NREM sleep state.

https://doi.org/10.1038/s41467-025-66436-x

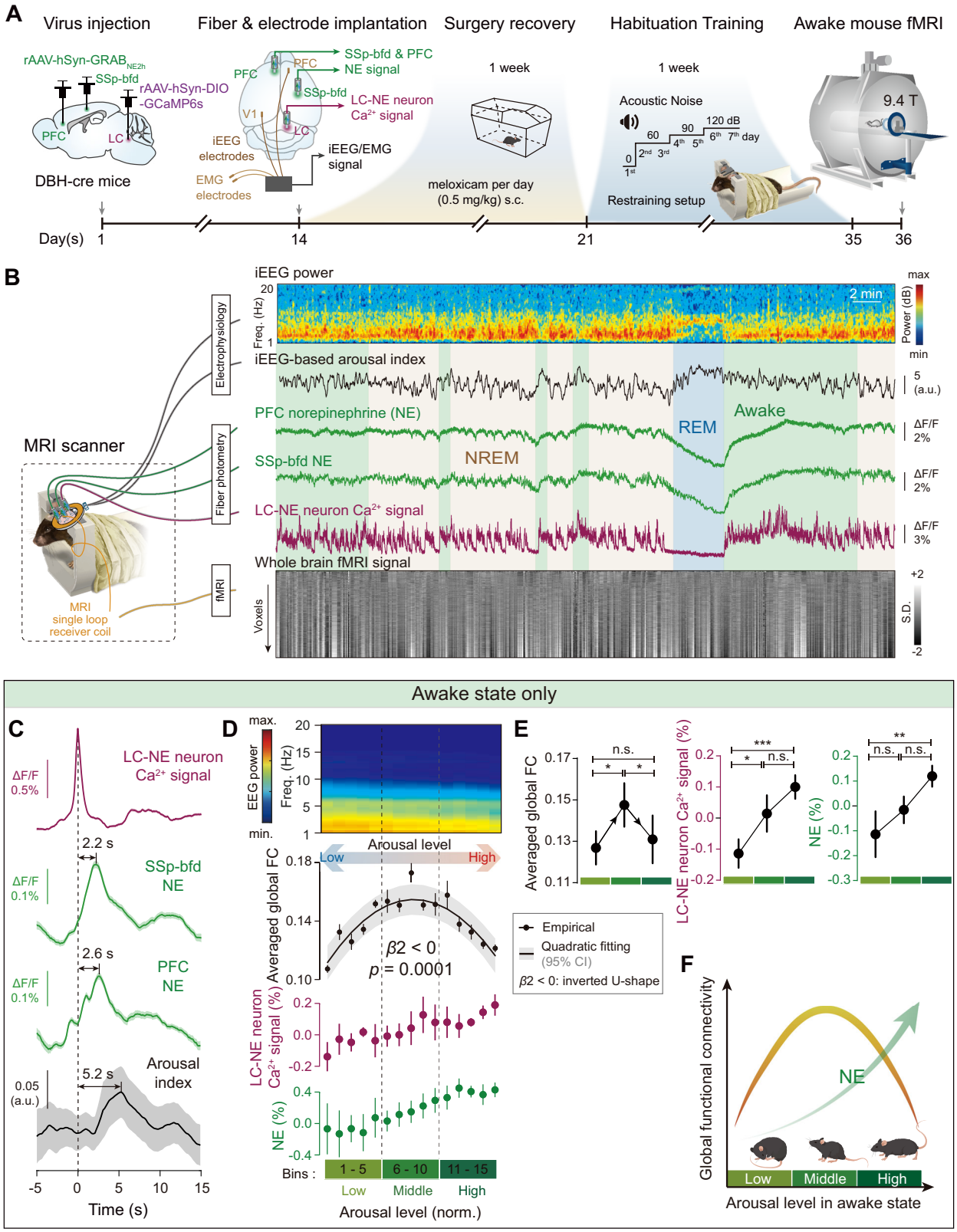


Our cross-species comparison relied on species-specific EEG-based arousal indices in awake periods (EEG α/θ in human awake EEG-fMRI, and 2–10 Hz inverse power in mice), which differ in spectral definitions. In the awake state, both human scalp EEG and mouse intracranial EEG primarily reflect synchronous postsynaptic currents from large pyramidal ensembles. However, the differences between physiology and recording setup (human scalp EEG v.s. mouse intracranial EEG) influence which electrophysiological characteristic is most "visible" in the spectrum. Specifically, human scalp EEG is a far-field measurement with strong spatial and frequency low-pass filtering, favoring widespread, slow rhythms. And, the posterior alpha around ~10 Hz emerges as the dominant, arousal-sensitive rhythm in the spectrum. So, posterior alpha (~7–13 Hz) is a reliable marker of alertness and attention[42], whereas frontal or central theta (~3–7 Hz) rises

**Fig. 4 | Cortical NE concentration and LC-NE neuronal activity were related to arousal-modulated whole-brain FC. A** Schematic setup and experimental timeline of multimodal awake mouse fMRI. Intracranial EEG (iEEG), electromyography (EMG), LC-NE neuronal calcium signal using GCaMP6s, and cortical extracellular NE signals using $GRAB_{NE\text{-}2h}$ were simultaneously recorded during awake mouse fMRI. Data from $N = 8$ mice. Among the data, 6 sessions included LC-GCaMP photometry, and 4 sessions included cortical $GRAB_{NE\text{-}2h}$ photometry. All sessions included iEEG recordings. **B** Representative traces of mouse iEEG power spectrum, iEEG-based arousal index, PFC NE concentration, SSp-bfd NE concentration, LC-NE neuronal calcium signal, and whole-brain BOLD signals. (N)REM (non-)rapid eye movement. **C** Peaks of LC-NE neuronal calcium signal lead to time-delayed elevation of extracellular NE concentrations and iEEG-based arousal index. ($n = 610$ episodes). Error bar, the standard error of the mean (SEM). **D**, **E** Inverted U-shaped relationship between mouse whole-brain FC dynamics and arousal level in awake state. With the increases of arousal level, there was a corresponding gradual elevation of LC-NE neuronal calcium signal and cortical NE sensor signals. Error bar, the SEM. Statistical significance was determined by the one-sample *t*-test (**D**, two tails, $n = 8$ runs for each bin) or paired *t*-test (**E**, two tails, $n = 5$ bins for each arousal level). n.s. no significance; **, $p < 0.01$; ***, $p < 0.005$; ****, $p < 0.001$. **F** Schematic summary of the inverted U-shaped relationship between NE and whole-brain FC. Source data are provided as a Source Data file.

with drowsiness[43]. The alpha/theta ratio normalizes inter-individual background and amplifier differences and is widely used as a continuous arousal/alertness index in human EEG and human EEG-fMRI studies[13,27,43,44]. For the mouse intracranial EEG in our study, the smaller brain and near-source intracranial EEG (iEEG) preserve more local activity, and the iEEG signal is dominated by low-frequency fluctuations without apparent fluctuations in alpha bands during quiet wake periods. Such low-frequency fluctuations are rapidly suppressed with increasing arousal, such as locomotion and pupil dilation[1,40,41]. Consequently, for the awake state, applying the human EEG-based arousal index, i.e., alpha/theta ratio, to mice could not precisely capture the arousal fluctuations due to the absence of apparent alpha rhythms in mouse intracranial EEG. It is worth to emphasize that such definitions of arousal indices have been commonly used in previous humans and mice EEG studies[1,13,27,40,41,43,44], respectively.

Thus, to verify the validity of EEG-based arousal indices for humans and mice in awake state, we utilized the well-established proxy of arousal, i.e., pupil size, for both humans[22,45,46] and mice[1,40,41]. In our study, the monotonic increase of pupil size along with increasing arousal index in humans (Fig. 1G, H) resembled that in mice (Supplementary Fig. 8C, D). Thus, while the EEG-based arousal indices between mice and humans differ in spectral bands, we believed that they both represented the arousal fluctuations. Nevertheless, more detailed cross-species evaluation of arousal index definitions will be beneficial for future studies.

It is worth to note that our LC-NE manipulation experiments and arousal-FC analyses (Figs. 5–7) were designed in a causal manipulation framework, and the key inference (Fig. 8) was anchored to each session's pre-manipulation baseline and to the direction of arousal change relative to that baseline. We intentionally did not z-score the arousal index, because the baseline-dependent interpretation requires a physiologically meaningful pre-manipulation baseline arousal index. Normalizing of EEG-based arousal index across sessions would obscure absolute baseline differences that are critical to the baseline-dependent effects. For example, normalizing the EEG-based arousal index in anesthetized mice could lead to the pre-manipulation baseline level center in the middle arousal, which is clearly not correct for anesthetized state.

Indeed, absolute baseline arousal values varied across mice and sessions, due to individual variability in the whole experimental pipeline, including electrophysiological setup and individual arousal states. However, it is worth to emphasize that the definition of low, middle, and high levels was based on the trisected full awake-only arousal spectrum from mouse resting state EEG-fMRI. And, in awake mice the baseline arousal levels across mice during pre-manipulation periods were randomly distributed across the full spectrum of arousal level. Thus, despite the individual variability, the group-averaged arousal index for awake mice during pre-stimulation periods should approximate the mean of the awake-only arousal distribution, i.e., middle arousal level in the inverted U-shape (Figs. 5G and 6G). Similarly, the group-averaged arousal index pre-chemogenetics for anesthetized mice approximated the low arousal level in the inverted U-shape (Fig. 7). Therefore, we believed that it is reasonable to qualitatively define the baseline arousal level as middle level for awake mice and low level for anesthetized mice (Figs. 5–7).

Importantly, our work resolved the discrepancy of how arousal level modulated FC dynamics. Our results revealed an inverted U-shaped relationship between global FC and arousal (Fig. 8), therefore, increased arousal level may both increase and decrease FC strength depending on the baseline arousal conditions. For example, previous chemogenetic LC-NE activation in anesthetized mice induced FC increases[20,21], as isoflurane anesthesia suppresses LC firing and achieves low baseline arousal level (Fig. 7). Thus, under such low arousal condition, increased LC-NE activity led to increased global FC and arousal changes from low to middle level (Fig. 8, the left half of the inverted U-shape). By developing the awake mouse iEEG-fMRI platform preserving physiological arousal fluctuations[24], full arousal spectrum can be observed, which enabled cross-species comparison with human EEG-fMRI. In addition to the capability of observing full arousal spectrum, another key advantage of our awake mouse iEEG-fMRI platform is the invasive recording and precise manipulation of LC-NE neurons. Combining fiber photometry recording and opto-/chemo-genetics manipulations of LC-NE neurons (Figs. 5–7), our results revealed LC-NE causally drove the inverted U-shaped FC dynamics, depending on the initial baseline arousal level (Fig. 8). Therefore, such nonlinear relationship in our results reconciled the previous discrepancy of arousal-modulated FC changes.

Meanwhile, this non-monotonic arousal-FC relationship indicates that global FC alone is not a one-to-one biomarker of absolute arousal across full arousal spectrum, and it is essential to extract other features of whole-brain FC dynamics to develop an fMRI only arousal index. Our work provided more evidence of arousal modulation on FC dynamics, emphasizing the necessity of arousal monitoring during fMRI using pupil size, EEG and/or other arousal behavioral markers.

Our experiments demonstrated the sufficiency, i.e., LC-NE manipulations modulate global FC in a baseline-dependent manner. However, given the interconnections within the ascending arousal system, global FC is unlikely to be only modulated by LC-NE system, and LC-NE manipulations in the current study could also involve other pathways, such as dopaminergic, cholinergic, serotonergic circuits. To further investigate the roles of other neuromodulatory systems in LC-NE manipulations, future work will be needed to record and perturb other neuromodulatory nodes (e.g., VTA, basal forebrain, dorsal raphe) in parallel using EEG, opto-/chemo-genetics, pharmacological antagonists, and fiber photometry to quantify co-fluctuations of arousal and FC dynamics. Combining such multimodal information could provide a more comprehensive assessment of neuromodulatory-specific contributions to the inverted U-shaped FC dynamics in the future.

Recent studies have emphasized that dynamic resting-state fMRI connectivity may reflect structured spatiotemporal co-fluctuations, which were accompanied by spontaneous arousal events[47–49], such as pupil dilations and other behavioral consequences. Thus, the arousal-related inverted U-shaped global FC dynamics we reported could also be interpreted as arousal-dependent reshaping of large-scale co-fluctuations, consistent with the observation that regions showing strong

https://doi.org/10.1038/s41467-025-66436-x

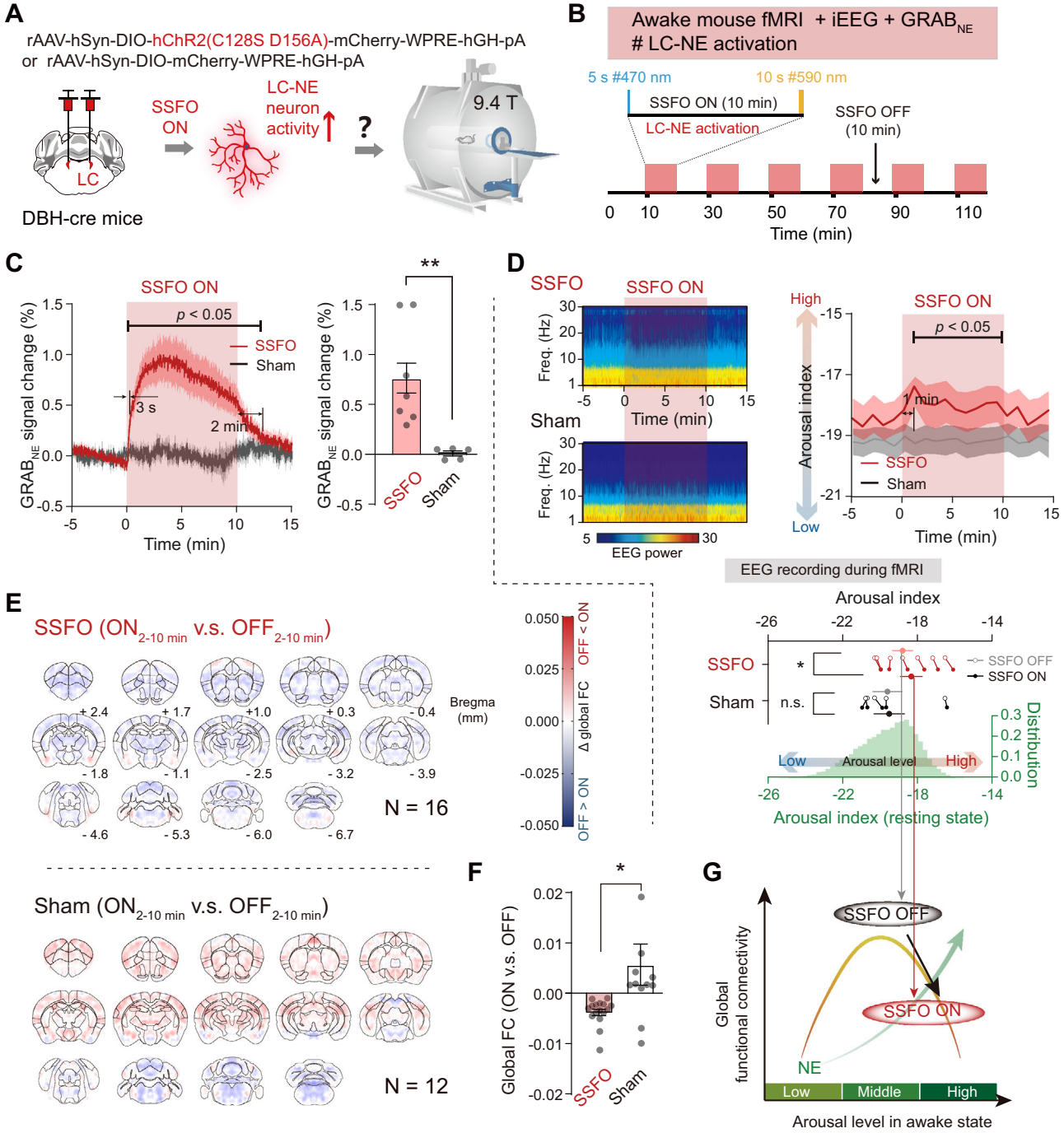


**Fig. 5 | Optogenetic excitation of LC-NE neurons increased arousal level and decreased whole-brain FC in awake mice. A**, **B** Schematic setup of awake mouse fMRI with simultaneous recording of iEEG and NE fiber photometry under stabilized step-function opsin (SSFO)-based optogenetic activation of LC-NE neurons. **C** SSFO activation of LC-NE neurons significantly increased cortical extracellular NE concentrations. Error bar or shades, the standard error of the mean (SEM). Each dot represented an individual mouse ($N = 7$ mice for SSFO & $N = 5$ mice for Sham). Statistical significance was determined using two-tailed two-sample $t$-test. **, $p < 0.01$. **D** SSFO activation of LC-NE neurons promoted the significant increase of arousal from middle to high level in awake mice. Upper left, averaged iEEG power spectrum in SSFO and Sham groups. Upper right, significant increase of mouse arousal level of SSFO group, compared to that of Sham group. Here, we computed the EEG-based arousal index in 60 s window width (non-overlapping) to maximize SNR and to align with the slower FC measures used in the group analysis. Notably, such choice limited the detectable transition time to 1 min, and the results processed with higher temporal resolution were shown in Supplementary Fig. 12. Lower, SSFO activation of LC-NE neurons increased the arousal from middle to high level in awake mice. Each line represented an individual mouse ($N = 7$ mice for SSFO & $N = 5$ mice for Sham). Error bar, the SEM. Statistical significance was determined using (two tails) paired $t$-test. *, $p < 0.05$. n.s. no significance. **E**, **F** SSFO activation of LC-NE neurons decreased whole-brain FC in awake mice. Each dot represented an individual mouse ($N = 16$ mice for SSFO & $N = 12$ mice for Sham). Error bar, the SEM. Statistical significance was determined using two-tailed two-sample $t$-test. *, $p < 0.05$. **G** Schematic summary of increased arousal from middle to high level and decreased whole-brain FC after SSFO activation on LC-NE neurons in awake mice. Source data are provided as a Source Data file.

https://doi.org/10.1038/s41467-025-66436-x

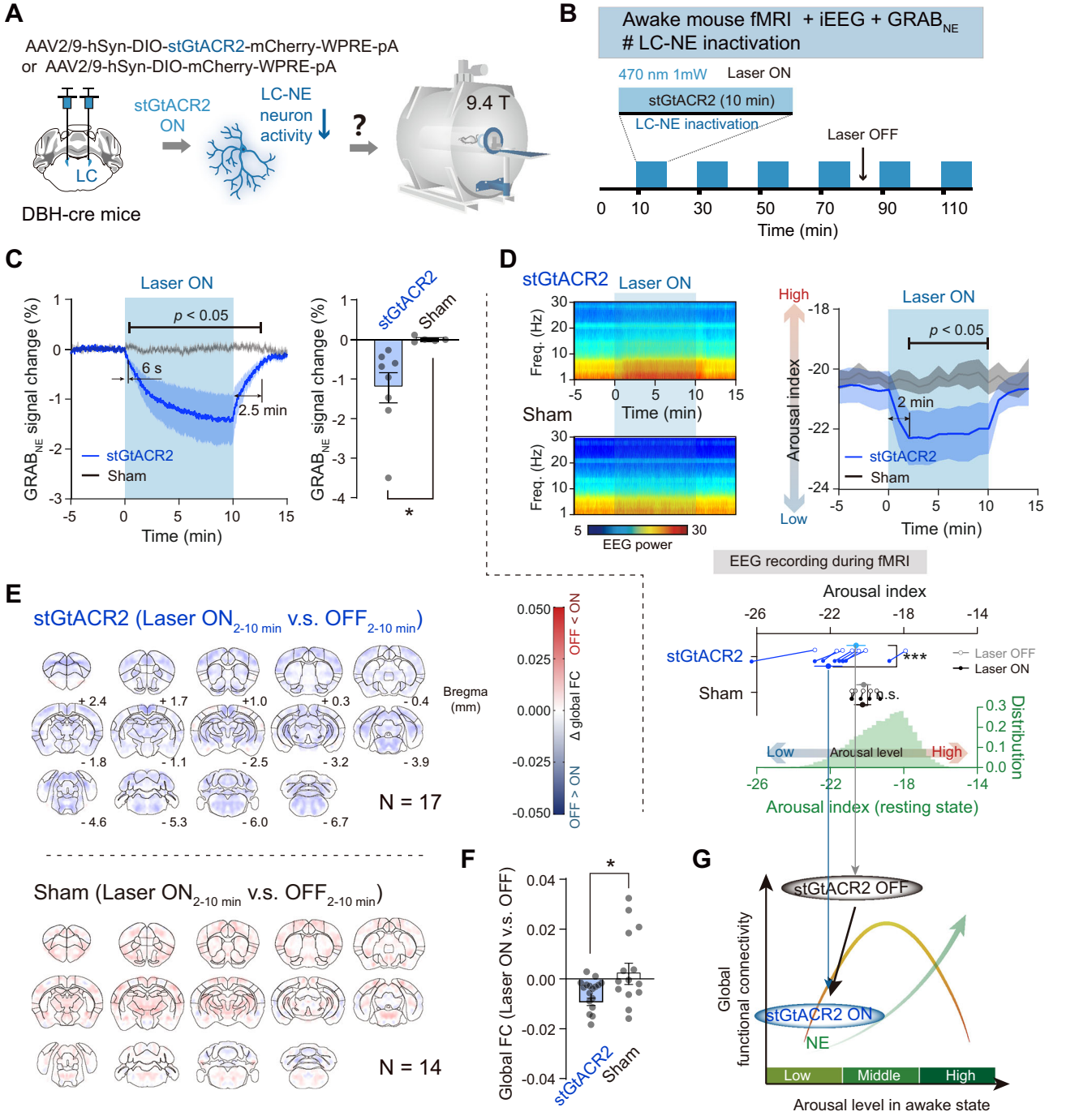


**Fig. 6 | Optogenetic inhibition of LC-NE neurons decreased both arousal level and whole-brain FC in awake mice. A**, **B** Schematic setup of awake mouse fMRI with simultaneous recording of iEEG and NE fiber photometry under stGtACR2-based optogenetic inactivation of LC-NE neurons. **C** stGtACR2-based inactivation of LC-NE neurons significantly decreased cortical extracellular NE concentrations. Error bar or shades, the standard error of the mean (SEM). Each dot represented an individual mouse ($N = 8$ mice for stGtACR2 & $N = 5$ mice for Sham). Statistical significance was determined using two-tailed two-sample $t$-test. **, $p < 0.01$. **D** stGtACR2-based inactivation of LC-NE neurons promoted the significant decrease of arousal from middle to low level in awake mice. Upper left, averaged iEEG power spectrum in stGtACR2 and Sham groups. Upper right, significant decrease of mouse arousal level of stGtACR2 group, compared to that of Sham group. Here, we computed the EEG-based arousal index in 60 s window width (non-overlapping) to maximize SNR and to align with the slower FC measures used in the group analysis. Lower, stGtACR2-based inactivation of LC-NE neurons decreased the arousal from middle to low level in awake mice. Each line represented an individual mouse ($N = 8$ mice for stGtACR2 & $N = 5$ mice for Sham). Error bar or shade, the SEM. Statistical significance was determined using two-tailed paired $t$-test. ***, $p < 0.005$. n.s. no significance. **E**, **F** stGtACR2-based inactivation of LC-NE neurons decreased whole-brain FC in awake mice. Each dot represented an individual mouse ($N = 17$ mice for stGtACR2 & N = 14 mice for Sham). Error bar, the SEM. Statistical significance was determined using two-tailed two-sample $t$-test. *, $p < 0.05$. **G** Schematic summary of decreased arousal from middle to low level and decreased whole-brain FC after stGtACR2-based inactivation on LC-NE neurons in awake mice. Source data are provided as a Source Data file.

https://doi.org/10.1038/s41467-025-66436-x

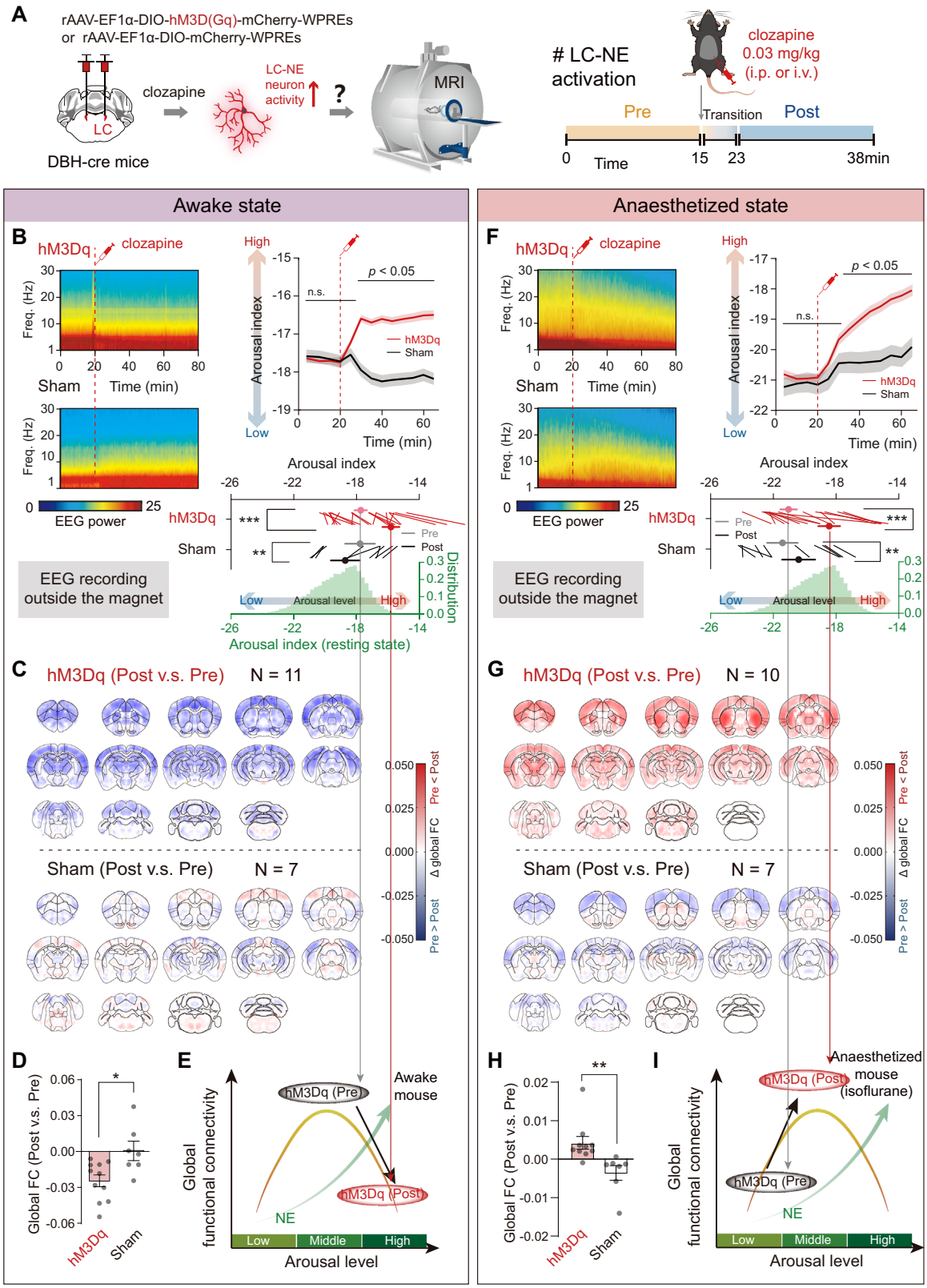


FC modulation (sensorimotor, LC, BF, SNr, and DR in Fig. 3G) also participated prominently in infra-slow traversing propagations of neural activities[50]. Future work could extend the analysis to explicitly quantify how the occurrence, spatial topology, and phase of such patterns varied with arousal and LC-NE activity.

While the arousal effect is generally considered to be global, the regionally specific effect still exists. Neurocircuitry studies[51–53] have identified that LC-NE mediated arousal enhanced thalamocortical transmission, strengthened corticocortical connectivity in prefrontal networks. Nevertheless, in the current study, the approach of averaging FC with other regions[54] provided a convenient view of FC dynamics and highlighted a global perspective on how arousal modulates FC changes across whole-brain. Even though such averaging approach partially obscured region-level information, the regionally

**Fig. 7 | Direction of FC changes within the inverted U-shaped pattern under LC-NE activation was dependent on the baseline arousal level. A** Schematic setup of mouse fMRI under hM3Dq-based chemogenetic excitation of LC-NE neurons for both awake and anaesthetized states. **B** Chemogenetic activation of LC-NE neurons promoted significant increase of arousal from middle to high level in awake mice. Upper left, averaged iEEG power spectrum in hM3Dq and Sham groups. Upper right, significant increase of mouse arousal level of hM3Dq group, compared to that of Sham group. Lower, chemogenetic activation of LC-NE neurons increased the arousal from middle to high level in awake mice. Here, iEEG recording with chemogenetics was conducted outside the magnet. Each line represented an individual mouse ($N = 22$ mice for hM3Dq & $N = 9$ mice for Sham). Error bar, the standard error of the mean (SEM). Statistical significance was determined using (two tails) paired $t$-test. *, $p < 0.05$. n.s. no significance. **C**, **D** Chemogenetic activation of LC-NE neurons decreased whole-brain FC in awake mice. Each dot represented an individual mouse ($N = 11$ mice for hM3Dq & $N = 7$ mice for Sham). Error bar, the SEM. Statistical significance was determined using (two tails) two-sample $t$-test. *, $p < 0.05$. **E** Schematic summary of increased arousal from middle to high level and decreased whole-brain FC after chemogenetic activation on LC-NE neurons in awake mice. **F**–**H** Similar to (**B**–**D**) but for isoflurane anaesthetized mouse (iEEG: $N = 15$ mice for hM3Dq & $N = 10$ mice for Sham, fMRI: $N = 10$ mice for hM3Dq & $N = 7$ mice for Sham). Chemogenetic activation of LC-NE neurons promoted significant increase of arousal from low to middle level and whole-brain FC in anaesthetized mice. **$p < 0.01$. Functional MRI data[20] was obtained from Zerbi. et al. **I** Schematic summary of increased arousal and whole-brain FC after chemogenetic activation on LC-NE neurons in anaesthetized mice. Source data are provided as a Source Data file.

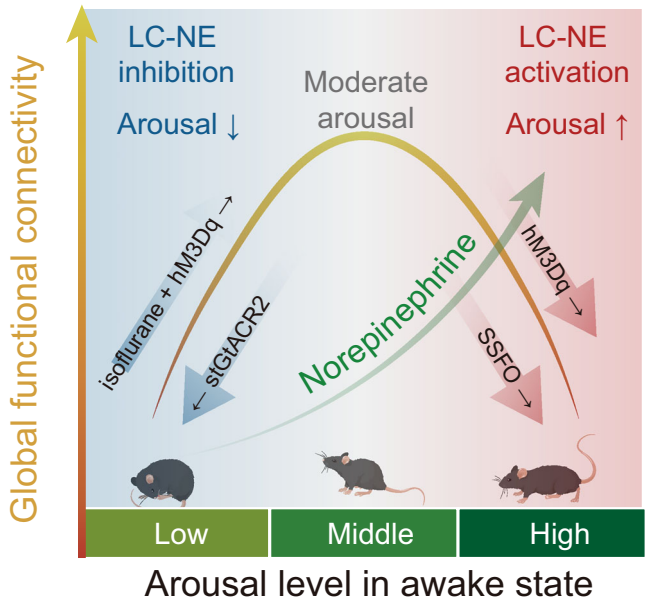


**Fig. 8 | LC-NE mediated arousal fluctuations drive inverted U-shaped functional connectivity dynamics.** LC-NE activity and resulting extracellular NE concentrations increased with arousal in awake state, and contributed to the inverted U-shaped global FC dynamics. Based on up and downregulations on LC-NE neurons, the baseline arousal largely determined the NE-mediated inverted U-shaped global FC dynamics.

specific effect of arousal modulated FC dynamics could still be observed (Fig. 3). Moreover, this global perspective broadened the current understanding of NE as a neuromodulator, transitioning from a circuit framework to a whole-brain view that recognizes its role in driving arousal state dynamics, ultimately influencing behaviors.

While we are confident that inverted U relationship between arousal and global FC is valid in both species, whether such inverted U relationship has the same underlying neural mechanism at neuronal or circuitry level is unclear. To investigate such cross-species neural mechanisms will be a challenging task to address. First, the neural mechanism of FC itself has been examined by many previous studies[13,55–58] and yet a consensus has not been reached. Such difficulty may in part attribute to the fact that FC is highly dynamic and influenced by many factors, such as arousal, and FC dynamics in different brain states may reflect different neural substrates. Therefore, it will be beneficial for future studies to examine the neural mechanism of FC in dynamically and specifically defined states, rather than treating FC as a static measurement across a time scale of several minutes. Such in-depth understanding of neural mechanism of arousal-modulated FC will likely to be achieved in animal studies first, with numerous invasive methods available, and then gradually tested in human as well. In short, caution should be exercised when interpreting the potential neural substrates of cross-species inverted U relationship.

Critically, awake mouse imaging across arousal states faces the challenge of two closely related factors, head motion and stress level. The current awake mouse fMRI setup has been systematically optimized to reduce stress level, achieving NREM and REM sleep during fMRI[24] (Fig. 4B). Head motion and physiological fluctuations are known to be intricately related to arousal. Our preprocessing step, involving extraction and regression of principal components (PCs) from non-brain fMRI signals (Supplementary Fig. 1), effectively suppressed non-neuronal signals, such as head motion, scanner drift, and physiological effects[12,23,24] (Supplementary Figs. 1–3). Additional analysis with global signal regression (GSR) (Supplementary Fig. 4) further supported the robustness of the inverted U-shaped relationship. Nevertheless, motion was also reported to be linked to micro-arousal and related to neuronal signal changes[59], which is one of the neural contributors to the whole-brain FC caused by arousal[56]. Notably, the same inverted U-shaped relationship was recapitulated using the calcium-based FC in awake mice (Supplementary Fig. 8), which is independent of BOLD hemodynamics. Therefore, the converging evidence (Supplementary Figs. 4 and 8) indicated that the observed inverted U-shaped arousal-FC relationship was very unlikely to be artifactually driven by the motion or physiological changes.

Given the complexity of the current multimodal awake mouse fMRI setup with iEEG and fiber photometry, the quality of functional images with regards to both SNR and image distortion was inevitably affected. Nevertheless, we demonstrated the data quality (Supplementary Fig. 5) was sufficient for our purpose. Future technical development for improved MR compatibility of simultaneous electrophysiological and fiber photometry recording will help to mitigate this issue. One limitation in this study was that we did not directly measure LC-NE neuron firing rates during manipulation. Nevertheless, the temporal coupling between $GRAB_{NE\text{-}2h}$ signals, iEEG-based arousal indices, and FC changes (Figs. 5D and 6D) strongly supports the physiological relevance of our manipulations. Another limitation was that the sham cohort for the anesthetized state showed small increases in arousal (Fig. 7F) and decreases in FC (Fig. 7H), and was not consistent with the inverted U-shaped pattern predicted from LC-NE activation. First, the changes of arousal in the sham group were smaller than those for experimental group. Such subtle variations might arise from that the anesthetized chemogenetic fMRI data (from Zerbi's group, the published dataset from ref. 20) and electrophysiology data (newly acquired in our group) were from different laboratories using not completely identical anesthetized and physiological setups, even with our best efforts to ensure consistency. It is worth emphasizing that, within our in-house preparations, bidirectional optogenetic manipulations of LC-NE neurons in awake mice fMRI (Figs. 5 and 6) yielded the expected opposite FC changes for arousal increases versus decreases, which was the core evidence supporting our conclusions.

## Methods

### Human detection task fMRI dataset

The human detection task fMRI dataset[22] was obtained from the OpenNeuro platform (ds001242). The study enrolled 28 healthy younger adults (Mean age = 24.39 years, age range = 18–34; 9 females) and 24 healthy older adults (Mean age = 66.95 years, age range = 55–75; 9 females). Participants provided informed consent approved by the University of Southern California Institutional Review Board and were paid for their participation. The experiments comprised several scanning sessions, but we only used anatomical scan and spatial detection task scans in the current analysis. MRI data were acquired using a 3 T Siemens Magnetom Trio scanner. Anatomical image were acquired using a magnetization-prepared rapid acquisition gradient echo (MPRAGE) sequence with the following parameters: repetition time (TR) = 1950 ms, echo time (TE) = 2.26 ms, flip angle (FA) = 7°; field of view (FOV) = 256 mm, resolution = 1 × 1 × 1 $mm^3$. Functional images for spatial detection task were acquired using an echo planar imaging (EPI) sequence with 139 volumes using the following parameters: TR = 2000 ms, TE = 25 ms, FA = 90°; matrix size = 64 × 64, in-plane resolution = 4 × 4 $mm^2$, slice thickness = 4 mm (interleaved, no skip), and number of slices = 41.

Briefly, two auditory tones (500 Hz and 800 Hz) served as conditioned shocks (CSs). For the spatial detection task, each trial began with simultaneous presentation of a fixation cross and either the CS+ or CS− tone. The tone was played for 0.7 s, then the fixation cross remained on the screen for an additional 2 s. Next, a pair of images, i.e., one depicting a place and the other an object, were displayed in placeholder frames simultaneously for 0.6 s. The salient image had a higher contrast level (80%) than the paired non-salient image (20%). And to further increase its salience, it was highlighted with a yellow border for 0.1 s. Participants were required to identify the location of the salient image. The inter-trial interval was randomly jittered (2.5, 3.5, 4.5, and 5.5 s). For each run, 16 CS+ trials (8 place salient and 8 place non-salient trials) and 16 CS− trials presented in a random order. Across five runs, a total of 160 trials were conducted. Pupil diameter changes were recorded simultaneously at a 60 Hz sampling rate.

### Human simultaneous EEG–fMRI dataset of natural sleep

The human sleep EEG-fMRI dataset was obtained from the OpenNeuro platform (ds003768) and acquisition details can be found in the original publication[26]. Briefly, this data enrolled 33 healthy participants (age: 22.1 ± 3.2 years; male/female: 17/16) with provided informed written consent. All experimental procedures have been approved by the Institutional Review Board at the Pennsylvania State University. The experiments comprised several scanning sessions, and we only used the data from the anatomical scan, two 10-min resting state scans, and several 15-min sleep scans. The participants' eye states were monitored during the scanning. Participants were instructed to press a button on a joystick approximately once per second as a behavioral measurement of wakefulness. They were allowed to stop the button pressing as they felt falling asleep.

MRI data were obtained using a 3 T Siemens Prisma scanner. Anatomical image was acquired using a MPRAGE sequence with the following parameters: TR = 2300 ms, TE = 2.28 ms, inversion time (TI) = 900 ms; FA = 8°; FOV = 256 mm, resolution = 1 × 1 × 1 $mm^3$, and acceleration factor = 2. Functional images were acquired using an EPI sequence with the following parameters: TR = 2100 ms, TE = 25 ms, FA = 90°; FOV = 240 mm, in-plane resolution = 3 × 3 $mm^2$, slice thickness = 4 mm, and number of slices = 35. The 32-channel EEG data were simultaneously collected at a sampling rate of 5000 Hz with a passband of 0–250 Hz. Sleep stages have been classified based on EEG signatures determined by a Registered Polysomnographic Technologist according to the AASM-recommended EEG exploratory derivations.

### Mouse sleep fMRI dataset

The simultaneous electrophysiology and fMRI dataset in non-anesthetized mice was obtained from our previous study[24]. In total, 46 sessions of 4-h simultaneous ECoG/LFP-fMRI were recorded from 24 wild-type C57BL/6J mice. The neurophysiological signals were sampled at a rate of 24414 Hz with a high-pass filtering at 0.1 Hz and notch filtering at 50, 100, and 150 Hz to mitigate noise. MRI trigger signals were recorded simultaneously at a sampling rate of 1024 Hz. All MRI data were acquired with a Bruker BioSpec 9.4 T scanner. An 86 mm volume coil was utilized for transmission and a 1 cm diameter single loop head coil was used for receiving. Mouse was head-fixed as described in our previous study[24] with no anesthesia. A T2-weighted anatomical image was acquired for coregistration purpose using a rapid acquisition with relaxation enhancement (RARE) sequence with the following parameters: TR = 3200 ms, TE = 34 ms, matrix size = 256 × 128, FOV = 18 × 9 $mm^2$, slice thickness = 400 μm, in-plane resolution = 70 × 70 $μm^2$, and number of slices = 22. After local shimming using Mapshim, functional images were acquired using an EPI sequence with the following parameters: TR = 2000 ms, TE = 14 ms, FA = 70°, matrix size = 90 × 45, nominal in-plane resolution = 200 × 200 $μm^2$, slice thickness = 400 μm, number of slices = 22, and 7200 EPI volumes. All 7200 volumes (4 h) were collected in a single EPI scan.

### Mouse wide-field calcium imaging dataset

The mouse wide-field calcium imaging data were adopted from a previous study[31]. This dataset included 8 Thy1-GCaMP6s transgenic adult male mice (JAX024275), which express the calcium indicator GCaMP6s in excitatory pyramidal neurons. To effectively eliminate the hemodynamics signals, the 470 nm excitation light and 405 nm light were alternately applied frame by frame. The fluorescence acquired under the 405 nm light served as the control, as it is largely independent of the calcium concentration.

The wide-field imaging data were captured at a sampling frequency of 20 Hz for each wavelength (Supplementary Fig. 8A). An infrared camera was utilized for tracking the mice's pupil and facial whisker movements. EEG and electromyogram (EMG) signals were recorded at a sample rate of 1000 Hz with low-pass filtering below 200 Hz. In total, 19 sessions of wide-field imaging recording were collected. The states of Wake, NREM sleep, and REM sleep have been manually classified based on EEG/EMG characteristics[31]. The wide-field calcium imaging data have been preprocessed, including (1) motion correction, (2) hemodynamics correction, and (3) registration to the CCFv3 mouse brain atlas.

### Animals

For all data acquired in this study, all mouse experiments were approved by the Animal Care and Use Committee of the Institute of Neuroscience, Chinese Academy of Sciences, Shanghai, China. DBH-cre mice (MMRRC #032081-UCD STOCK Tg(Dbh-cre) KH212Gsat/Mmucd) were used for targeted expression of AAV virus in norepinephrine (NE) neurons in locus coeruleus (LC) for awake mouse fMRI experiments. Mice were group-housed (5–6/cage) in the standard laboratory condition (temperature: 23 ± 1 °C; humidity: 50–70%) under a 12-h light/dark cycle (light on from 7 a.m. to 7 p.m.) with food and water *ad libitum*. Experiments were conducted at 8–10 weeks of ages, weighted 18–30 × *g* for both male and female mice. Considering the study was designed to identify a cross-species mechanism of the inverted U-shaped relationship between arousal and global FC, sex of mice was not considered a primary variable of interest. Number of mice used in each experiment was detailed in the Table 1. No statistical method was employed to predetermine sample sizes, but the sample size in this study was similar to our previous publication[23].

**Table 1 | Summary of number of DBH-cre mice used in each fMRI experiment**

| | Fiber photometry (Fig. 4) | Optogenetics | | Chemogenetics |
|---|---|---|---|---|
| | | SSFO-based activation (Fig. 5) | stGtACR2-based inactivation (Fig. 6) | hM3Dq-based activation (Fig. 7) |
| iEEG + fMRI + X (single loop coil) | 8 | 7 for SSFO & 5 for Sham | 8 for stGtACR2 & 5 for Sham | / |
| fMRI + X (cryogenic coil) | / | 9 for SSFO & 7 for Sham | 9 for stGtACR2 & 9 for Sham | 11 for hM3Dq & 7 for Sham |

### Virus injection

All stereotaxic surgeries were performed under isoflurane anesthesia (4.5% for induction and ~1.5% for maintenance), and animals were placed on a stereotaxic frame with a heating pad (mouseSTAT, Kent Scientific Corporation). A midline sagittal incision was made along the scalp to expose the skull. Two craniotomies (~0.4 mm diameter) were made over bilateral LC (AP - 5.4 mm, ML ± 0.9 mm). Using the Nanoject III (Drummond Scientific) via a glass pipette, AAV viruses (Titer: $4.76 \times 10^{12}$ v.g./mL; BrainVTA Co., China) were injected separately (1 nL/s, 10 nL/cycle, inter-cycle interval 10 s, total 30 cycles and 0.3 μL) into each side of LC (AP − 5.4 mm, ML ± 0.9 mm, DV − 2.6 mm from dura), including rAAV-hSyn-DIO-GCaMp6s-WPREs for calcium optical fiber photometry; rAAV-hSyn-DIO-hChR2(C128S D156A)-mCherry-WPRE-hGH-pA and rAAV-hSyn-DIO-mCherry-WPRE-hGH-pA for SSFO-based optogenetics; AAV2/9-hSyn-DIO-stGtACR2-mCherry-WPRE-pA and AAV2/9-hSyn-DIO-mCherry-WPRE-pA for stGtACR2-based optogenetics; rAAV-EF1α-DIO-hM3D(Gq)-mCherry-WPREs and rAAV-EF1α-DIO-mCherry-WPREs for hM3Dq-based chemogenetics. Additionally, for the "iEEG + fMRI + X" experiments, we injected 0.5 μL rAAV-hSyn-NE2h-WPRE-hGH-polyA (Titer: $4.76 \times 10^{12}$ v.g./mL; BrainVTA Co., China) under the neuronal hSyn promoter[34,35] into unilateral prefrontal cortex (PFC) (AP + 1.7 mm, ML − 0.36 mm, DV − 1.3 mm from dura) and the barrel field of the primary somatosensory cortex (SSp-bfd) (AP − 1.43 mm, ML − 3 mm, DV − 0.54 mm from dura), respectively, to record cortical NE signals. After each injection, the needle was slowly pulled up following a 10-min waiting period to prevent backflow. Then, scalp was sutured, and mouse was placed in a postoperative incubator for anesthesia recovery.

### Implantation of optical fibers, electrodes, and head holder

Two weeks after the virus injection, we conducted the implantation of optical fibers, electrodes, and head holder for awake mouse fMRI[23,24]. Mice were pretreated with a subcutaneous (s.c.) injection of 5 mg/kg dexamethasone one hour before surgery. The scalp over the skull was removed, and the periosteum was cleared using cotton swabs moistened with 3 % hydrogen peroxide. The tissue covering the skull posterior to the lambda point was also removed for firmer anchorage for the head post. Then, the exposed skull was cleaned by saline. After drying the surface of skull, a coat of self-etch adhesive (3 M ESPE Adper Easy One) was applied, followed by blue light curing.

- Electrode and optical fiber implantation in "iEEG + fMRI + X" experiments

  Two bare silver wires (100 μm diameter; impedance, ~60 kΩ at 1 kHz) and six insulated gold wires (50 μm diameter; impedance, ~500 kΩ at 1 kHz) were soldered to a flexible flat cable[24]. Six 0.1 mm diameter holes were drilled in the skull. After that, four of the insulated gold wires were positioned on the dura to record intracranial EEG (iEEG) in the PFC (AP + 1.0 mm, ML − 1.0 mm), primary visual cortex (V1) (AP − 2.8 mm, ML + 2.5 mm), the trunk of the primary somatosensory cortex (SSp-tr) (AP − 1.34 mm, ML + 1.78 mm) and SSp-bfd (AP − 1.43 mm, ML + 3 mm), respectively. The remaining two gold wires were placed on nuchal muscles to record the electromyography (EMG) signals. The two bare silver wires were served as reference and ground electrodes, and inserted epidurally at ML = 0 mm, AP = −6.5 mm and −5.5 mm, respectively.

  To record extracellular NE concentrations, two silica optic fiber (0.2 mm diameter) embedded in a 1.25 mm ceramic ferrule (Thorlabs) was inserted into the PFC (AP + 1.7 mm, ML − 0.36 mm, DV − 1.2 mm from dura) and SSp-bfd (AP − 1.43 mm, ML − 3 mm, DV − 0.45 mm from dura), respectively. For calcium fiber photometry recording of LC-NE neurons, an additional silica optic fiber was inserted into unilateral LC (AP − 5.4 mm, ML + 0.9 mm, DV − 2.6 mm from dura).

  For optogenetic modulation of LC-NE neurons, we chose flexible fiber optic implants (200 μm in diameter; NA 0.5; Inper Co., China) made of poly-methylmethacrylate (PMMA) to insert into bilateral LC. The PMMA material has similar magnetic susceptibility to the brain tissue and thus could mitigate imaging artifacts typically caused by fiber implantation[23].

  To fix the electrodes and optic cannula to skull, we applied a light-curing flowable dental resin and cured it using the blue light for 20 s. A head holder for awake imaging[24] was then affixed to the skull above the cerebellum. Finally, dental cement was applied to smooth the surface of exposed skull, ensuring stable fixation of electrodes and the head holder.
- Optical fiber implantation in "fMRI + X" experiments

  For fMRI experiments with no iEEG recordings, flexible PMMA fibers were used to delivery lights to bilateral LC, to accommodate the limited space of the cryogenic RF coil that was later used in fMRI[23]. All other steps were consistent with those previously described. No silica optical fibers and $GRAB_{NE\text{-}2h}$ sensor were used in this part.

After surgery, mice were placed in a postoperative incubator for anesthesia recovery. Subsequently, mice were injected with meloxicam 0.5 mg/kg subcutaneously for 7 consecutive days to manage postoperative pain.

### Habituation for awake mouse fMRI

After 1-week recovery from the surgery, the mice underwent a 7-day habituation for awake fMRI scanning. During this period, mice were head-fixed on the animal bed with the recorded acoustic MRI scanning noise, following the paradigm detailed in our previous studies[23,24]. The schedule for the habituation training was outlined in Table 2. No reward was given during or after the habituation training.

### Acquisition of simultaneous iEEG-fMRI and fiber photometry in awake mice

MRI data were acquired with a Bruker BioSpec 9.4 T scanner at Brain Imaging Center, Institute of Neuroscience, Chinese Academy of Sciences. An 86 mm volume coil was used for transmission and a single loop head coil (Bruker, 2 cm diameter) was used for receiving. Mouse was head-fixed with no anesthesia. A thick layer of Kwik-cast was applied smoothly over the mouse skull immediately before the MRI scanning to reduce image distortion. A T2-weighted RARE anatomical image was acquired with the following parameters: TR = 3200 ms, TE = 33 ms, FA = 90°, matrix size = 128 × 128, FOV = 16 × 16 $mm^2$, slice thickness = 500 μm, in-plane resolution = 125 × 125 $μm^2$, number of slice = 28, RARE factor = 8, and average = 2. Functional images were acquired using gradient-echo EPI (GE-EPI) with the following parameters: TR = 2000 ms, TE = 15 ms, FA = 70°, matrix size = 90 × 60, in-

**Table 2 | Summary of habituation schedules for awake mouse fMRI**

| | Day 1 | Day 2 | Day 3 | Day 4 | Day 5 | Day 6 | Day 7 |
|---|---|---|---|---|---|---|---|
| Duration of habituation (min) | 60 | 90 | 120 | 120 | 120 | 120 | 120 |
| Acoustic noise (dB) | 0 | 60 | 60 | 90 | 90 | 120 | 120 |

plane resolution = 200 × 250 μm$^2$, slice thickness = 500 μm, number of slice = 28, dummy scan = 4, and 3750 EPI volumes (~2 h). All 3750 volumes were collected in a single EPI scan. Triggers were sent from the MRI console for each slice acquisition and recorded simultaneously with the iEEG/EMG signals to ensure precise temporal alignment between the imaging data and the physiological recordings. Additionally, two sets of GE-EPI with opposite phase-encoding directions were collected for EPI distortion correction (using the *topup* function in FSL) with the identical scanning parameters, but 8 volumes for each set.

During fMRI, iEEG/EMG signals were recorded simultaneously using the same procedure as previously described[24].

For simultaneous fiber photometry recording during fMRI, three 7-m optical fibers were connected to the LC, PFC, and SSp-bfd with sleeves, respectively. For each set of photometry setup, a 465 nm LED (CLED_465, Doric Lens) was used as excitation source, and a 405 nm LED (CLED_405, Doric Lens) was used as the control. Excitation power at the tip of the fiber was ~20 μW. The fluorescence detection was done by fluorescence optical mini cubes (FMC4_IE(400-410)_E(460-490)_F(500-550), Doric Lens) and the visible femtowatt photoreceivers (NPM_2151_FOA_FC, Doric Lens). A software-controlled lock-in detection algorithm was implemented using the TDT RZ2 system, employing the fiber photometry 'Gizmo' of the Synapse software (https://www.tdt.com/). The fiber photometry signals were recorded using the above TDT system at a sampling rate of 1017 Hz.

### Acquisition of optogenetics fMRI on LC-NE neurons in awake mice

For the optogenetics fMRI on LC-NE neurons, two 7-m fiber optic patch cables (200 μm in diameter; NA 0.5; Doric Lens) were used to deliver light into the bilateral LC with 470 nm or 590 nm laser (Shanghai Laser & Optics Century Co., Ltd.) placed outside the magnet room. Prior to the optogenetic fMRI experiment, mouse's eyes were covered with custom-made black eyepatches to avoid luminance-evoked arousal changes during awake imaging.

A T2-weighted RARE anatomical image was acquired with the following parameters: TR = 3300 ms; TE = 33 ms; matrix size = 256 × 256; FOV = 16 × 16 mm$^2$; slice thickness = 400 μm; in-plane resolution = 62.5 × 62.5 μm$^2$, number of slices = 35, FA = 90°, RARE factor = 8, and number of average = 2. Functional images were acquired using bi-band EPI with the following parameters: TR = 750 ms, TE = 15 ms, flip angle = 30°, bandwidth = 300 kHz, field of view = 15 × 12 mm$^2$, matrix size = 100 × 80, dummy scan = 10, nominal slice thickness = 0.48 mm (slice thickness 0.4 mm with a gap of 0.08 mm), 9700 volumes (~2 h), and 38 axial slices per scan. All 9700 volumes were acquired in a single EPI scan.

During fMRI, an Arduino Uno board (https://www.arduino.cc/) was utilized to synchronize the scanner trigger and the laser for optogenetic stimulations. To activate LC-NE neurons expressing the hChR2(C128S D156A), after 10-min baseline scanning, a blue light (470 nm, 1 mW) was administered for 5-s to turn on the SSFO, and 10-min later, SSFO was turned off by 10-s yellow light (590 nm, 1 mW). The above cycle was repeated 6 times for each EPI run. To deactivate LC-NE neurons expressing the stGtACR2 virus, continuous 10-min blue light (470 nm, 1 mW) was delivered to the bilateral LC after 10-min baseline scanning. The above cycle was repeated 6 times for each EPI run. The stimulation paradigms were illustrated in Figs. 5B and 6B, respectively.

In additional experiments (Figs. 5C–F and 6C–F), we combined the awake mouse optogenetics fMRI with simultaneous electrophysiology and fiber photometry, following the procedure described in "Acquisition of simultaneous iEEG-fMRI and fiber photometry in awake mice" section. MRI data was acquired using the same scanning parameters with the 2 cm diameter single-loop coil. During fMRI, same optogenetics stimulations were delivered to the bilateral LC of DBH-Cre mice with simultaneous iEEG recording and fiber photometry of extracellular NE concentration in PFC and (or) SSp-bfd.

### Acquisition of chemogenetics fMRI on LC-NE neurons in awake and anesthetized mice

For awake mouse fMRI with chemogenetic modulation on LC-NE neurons, the experimental paradigm was similar to those with optogenetics, but with no need for fiber implantation and light delivery. After 15 min of bi-band EPI acquisition with the cryogenic probe, a bolus of 0.03 mg/kg clozapine (HY-14539, MedChemExpress) was intraperitoneally (i.p.) injected to activate designer receptors exclusively activated by designer drugs (DREADDs). MRI parameters were identical to the optogenetic fMRI describe above, except total EPI volumes being 2800 (total EPI scanning time was 38 min).

Anesthetized mouse fMRI data with chemogenetics on LC-NE neurons was obtained from a previous study with experimental details described therein[20]. Briefly, in this dataset, 10 DBH-cre mice were injected with AAV5-hSyn1-DIO-hM3D(Gq)-mCherry in bilateral LC as the experimental group, and 7 mice were injected with AAV5-hSyn1-DIO-mCherry as the Sham group. MRI was performed using Bruker BioSpec 7 T scanner equipped with a cryogenic surface coil. Animals were endotracheally intubated and artificially ventilated. A bolus injection of muscle relaxant (pancuronium bromide, 0.2 mg/kg) was administered, and isoflurane was reduced to 1% for maintenance. For fMRI acquisition, a standard gradient-echo EPI sequence (TR = 1000 ms, TE = 15 ms, in-plane resolution = 0.22 × 0.2 mm$^2$, number of slice = 20, slice thickness = 0.4 mm, slice gap = 0.1 mm) was applied to acquire 2280 volumes in 38 min. After 15 min of GE-EPI acquisition, a bolus of 0.03 mg/kg clozapine was intravenously (i.v.) injected to activate DREADDs.

### Electrophysiological signal processing

The off-line correction of MRI gradient artifacts in the electrophysiological signals was identical to those in our previous study[24], which was conducted using the fMRI Artifact Slice Template Removal algorithm (FASTR)[60]. Briefly, the imaging artifact waveforms were segmented, averaged, and iteratively subtracted from the raw electrophysiological signals, based on the concurrently acquired trigger signal from the MRI scanner. This procedure was performed through FMRIB in EEGLAB. For the brain state classification, which followed the methodology from our previous study[24], one channel for each session was selected for further analysis. Briefly, spectral analysis was carried out using the fast Fourier transform, and brain states were classified based on established criteria into wake (wake: low delta power, low theta-to-delta ratio) and sleep states (NREM, synchronized EEG with high delta power and low neck EMG power; REM, high theta-to-delta ratio, low neck EMG power). Any epochs with short durations (<5 s) were manually merged to the nearest sleep stage.

Considering the potential systematic hemodynamic differences[28–30] across the awake-sleep cycle, we excluded the NREM and REM sleep states and only used awake state in both human and

animal (i)EEG-fMRI data in subsequent analysis. Electrophysiological signals were further used to characterize the arousal level during the awake state. In human data, the ratio of the power in the alpha band (7–13 Hz) to the theta band (3–7 Hz) was defined as the human EEG-based arousal index (Fig. 1), which aligned with the previous human EEG-fMRI study[27]. In mouse data, due to the distinct characteristics of EEG power spectrum between mice and humans, we used the inverse of the power in 2–10 Hz band[1] as mouse (i)EEG-based arousal index (Figs. 2, 4–7), achieving an accurate representation of mouse arousal index.

### Fiber photometry signal processing

Consistent with previous studies[61,62], we implemented a least-squares regression to regress the 405 nm control signal from the 470 nm fluorescence signal. The fluorescence changes were quantified as $(F-F_0)/F_0$, where F represented the fluorescence intensity at each time point and $F_0$ was the mean of fluorescence intensity. Finally, the fluorescence signal was downsampled to 1 Hz via the MATLAB function "*interp1*" and then used for the subsequent analysis.

### Human fMRI data preprocessing

To maximize the comparability across different human fMRI datasets, we selected to preprocess all datasets using the same pipeline, rather than utilizing the varied pipelines initially employed by the original studies. Preprocessing was performed based on Statistical Parametric Mapping 12 (SPM12) (http://www.fil.ion.ucl.ac.uk/spm/), implemented in MATLAB 2020a (MathWorks, Natick, MA). The preprocessing pipeline included the motion correction, normalization to Montreal Neurological Institute (MNI-152) standard space (2 mm isotropic resampling resolution), and spatial smoothing (isotropic 8 mm Gaussian kernel). Denoising approach was performed based on the "6 rp + 6 Δrp + 10 PCs" nuisance signal regression, which has been effectively applied to various fMRI datasets in rodents, non-human primates and humans in our previous studies[12,23,24,63] to minimize effects of scanner drift, motion and other non-neural physiological noises (Supplementary Fig. 1). The "6 rp + 6 Δrp" represented 6 head motion parameters and their 1st order first derivatives, and "10 PCs" were the first 10 principal components (PCs) derived from the BOLD signals of non-brain tissue, e.g., the muscles. To quantitatively assess the reduction of motion-related artifacts through these regressors, we calculated the Pearson's correlation coefficients between the frame-wise displacement (FD) and DVARS (D referring to temporal derivative of time courses, VARS referring to RMS variance over voxels). Then, the denoised BOLD signals were band-pass filtered (0.001–0.1 Hz) and normalized by subtracting its temporal mean and dividing by its temporal standard deviation on a voxel-by-voxel basis.

Preprocessing strategies have been shown to profoundly influence the resulting functional connectivity measurement. Therefore, in this study we systematically evaluated the results using different preprocessing approaches (Supplementary Fig. 4), i.e., "6 rp + 6 Δrp + 10 PCs", "6 rp + 6 Δrp", and "6 rp + 6 Δrp + WM + CSF + GSR", and found arousal modulated FC dynamics patterns (the inverted U shape) were largely preserved under different preprocessing (Supplementary Fig. 4). Therefore, the main human results reported herein were derived from the denoised dataset using the "6 rp + 6 Δrp + 10 PCs" regression approach.

### Mouse fMRI data preprocessing

For the mouse fMRI data, after the image format conversion, EPI distortion correction was conducted using the FSL's *topup*. The mouse brain was extracted manually utilizing ITK-SNAP (http://www.itksnap.org/). Subsequent procedures were performed utilizing custom scripts in MATLAB 2020a (MathWorks, Natick, MA) and SPM12 (http://www.fil.ion.ucl.ac.uk/spm/). For fMRI data acquired using the single-loop coil, principal component analysis (PCA) was applied to denoise EPI images by identifying the first N principal components (PCs) with high explained variance (> 0.05) and reconstructing the EPI images based on these N PCs. Then, Images of each EPI scan were registered to the scan-specific structural image utilizing the rigid body transformation, and the scan-specific structure image was nonlinearly transformed to the 3D Allen Mouse Brain Common Coordinate Framework, v3 (CCFv3, http://atlas.brain-map.org/) for group analysis. A light spatial smoothing (0.4 mm isotropic Gaussian kernel) was performed. After the preprocessing, the mouse fMRI data were further regressed by "6 rp + 6 Δrp + 40 PCs" nuisance signals, similar to that in "human fMRI data preprocessing". Considering the acquisition time for each mouse fMRI session was ~ 4 times as that in human fMRI dataset, we chose 40 PCs as nuisance regressors[24], instead of 10 PCs, to achieve better removal of non-neuronal nuisance effects. Finally, BOLD signals were band-pass filtered between 0.001 and 0.1 Hz and normalized by subtracting its temporal mean and dividing by its temporal standard deviation on a voxel-by-voxel basis.

### Arousal modulated dynamic functional connectivity

To reduce the computational load, we extracted mean time series from human fMRI data based on 1174 predefined regions of interest (ROIs), including 1000 cortical parcels using the Schaefer et al. human parcellation[64], 54 subcortical parcels defined by Tian et al.[65], 34 cerebellar regions from the atl-Anatom atlas[66], and 76 brainstem and 10 diencephalic nucleus from the Brainstem Navigator v1.0[67]. Notably, for the human detection task fMRI dataset, the task block structures were regressed out prior to the extraction of whole-brain time series to ensure unbiased dynamic FC analysis.

For the mouse fMRI data, mean time series were extracted from 15314 ROIs (7657 ROIs in each hemisphere) derived from a predefined partitioning[68]. Considering the bilateral nature of optogenetic and chemogenetic stimulations on LC-NE neurons, we averaged the BOLD signals between left and right hemispheres, resulting M (time points) × 7767 (parcels) for each EPI run. This approach preserved the detailed regional functional information while making large dataset analysis computationally feasible.

For the arousal modulated global dynamic FC, we firstly estimated dynamic FC, at the native fMRI resolution (i.e., each TR), using the dynamic conditional correlation (DCC) framework[25] (https://github.com/canlab/Lindquist_Dynamic_Correlation) on a parcel-by-parcel basis, which yields a time-varying correlation series at each TR without imposing long, fixed windows. Pairwise dynamic connectivity values were computed at every time point of each EPI run, resulting in a matrix of M (time points) × N (connections) per run. After the estimation of dynamic fMRI-based or calcium-based FC, arousal indices or behavioral markers were synchronized to scanner triggers, resampled to the fMRI TR or temporal resolution of calcium imaging, and then hemodynamic response function (HRF) -convolved or time-shifted to account for neurovascular delays before arousal-FC alignment, respectively. Specifically, we implemented species-specific lags in two ways: (i) convolving the EEG-based arousal indices with a species-specific HRF (humans: 5 s time-to-peak; mice: 2 s time-to-peak) and (ii) shifting behavioral markers, including button-pressing rate, pupil size, task performance, over small temporal offsets (humans: +5 s in TR steps; mice: +2 s in TR steps, reflecting the shorter mouse hemodynamic delay[61,63]). Last, to assess arousal modulated FC dynamics, we aligned and binned the dynamic FC matrices according to (i)EEG-based or pupil size-based arousal index with equal samples, yielding same degree of freedoms. After the binning, we averaged the FC samples in each bin. Thus, FC was not computed "within" short arousal bins; rather, binning was a subsequent averaging step that improves signal-to-noise ratio (Supplementary Fig. 2B).

For the preprocessed mouse wide-field calcium imaging data, we firstly separated the pixel-wise signals using unsupervised k-means clustering ($k = 100$) of Euclidean distances to reduce the computational loads. Then, the time series for each cluster was downsampled

from 20 Hz to 1 Hz. Next, the DCC approach was applied to the down-sampled time series across 100 clusters. Finally, the dynamic FC matrix (100 × 100 × M time points) was back-projected to the pixel-wise level, resulting (N pixels × N pixels × M time points).

### Histology and microscopy

To verify virus expression in specific cell types and the placement of optical fibers, mice were deeply anesthetized and transcardially perfused with 0.1 M phosphate-buffered saline (PBS) followed by 4% paraformaldehyde (PFA) in PBS. Brain tissues were removed and post-fixed overnight in 4% PFA. Subsequently, brains were transferred to a 30% sucrose solution at 4 °C for 48 h. Brain samples were embedded in OCT compound (NEG-50, Thermo Scientific) and cut into 50-μm sections using a cryostat (HM525 NX, Thermo Scientific). Sections were stored at −20 °C before processing. For immunohistochemistry, brain sections were incubated in primary antibody solution containing 0.2% Triton ×-100 and 2% normal goat serum in PBS at 4 °C with agitation for one night. After three 10-min washes in PBS, sections were transferred to secondary antibody solution (2% normal goat serum in PBS). Following three additional PBS washes, sections were mounted on glass slides and coverslipped with DAPI-containing mounting medium (F6057, Sigma). The primary antibodies used were mouse anti-TH (# SAB4502966, Sigma, 1:1000) and rabbit anti-NeuN (ABN78, Sigma, 1:1000). The secondary antibody used was Donkey Anti-Mouse Alexa Fluor 647 (#ab150107, Abcam, 1:300). Finally, fluorescence images were captured using a laser scanning confocal microscopy (Olympus FV3000).

### Significance test of spatial correlation using the spatial autocorrelation preserving shuffling

To address the spatial autocorrelation presented in the profiles of cell-type specific anterograde axonal tracing (Fig. 3I), we employed a shuffling procedure from previous studies[12,23,69] to enhance the accuracy of statistical significance assessment. The shuffling procedure has been fully described in our previous mouse and marmoset fMRI studies[12,23]. Briefly, we generated surrogate maps by randomizing their specific topographies 10000 times while maintaining the overall spatial autocorrelation structure. By using these surrogate maps to create null distributions, we determined the significance level, i.e., $p_{spin}$, of spatial correlation between axonal tracing map and the arousal modulated arousal modulated spatial pattern (Fig. 3I). This approach allowed us to account for intrinsic spatial dependencies and accurately evaluate the true statistical significance of the observed spatial correlations.

### Reporting summary

Further information on research design is available in the Nature Portfolio Reporting Summary linked to this article.

## Data availability

Simultaneous EEG–fMRI dataset of human natural sleep could be accessed via the link https://openneuro.org/datasets/ds003768/versions/1.0.9. Human detection task fMRI dataset could be accessed at https://openneuro.org/datasets/ds001242/versions/1.0.0. Mouse sleep fMRI dataset is openly accessible through Brain Science Data Center, Chinese Academy of Sciences at https://doi.org/10.12412/BSDC.1668502646.20001. Mouse wide-field calcium imaging dataset was deposited on ScienceDB and is available via the link https://doi.org/10.57760/sciencedb.17064. The mouse cell-type specific anatomical projections were from the Allen Mouse Brain Connectivity Atlas https://connectivity.brain-map.org/. The dataset of awake mouse iEEG-fMRI with simultaneous fiber photometry, optogenetics, and chemogenetics on LC-NE neurons were deposited on Brain Science Data Center, Chinese Academy of Sciences and is available via the link https://doi.org/10.12412/BSDC.1759022664.20002. The original chemogenetics fMRI dataset in anesthetized mice is available from corresponding authors of the original publication referenced herein[20]. Source data are provided with this paper.

## Code availability

Major codes for data analysis are available at https://github.com/TrangeTung/LC_inverted_U_shape_FNs.

## References


1. McGinley, M. J. et al. Waking state: rapid variations modulate neural and behavioral responses. *Neuron* **87**, 1143–1161 (2015).
2. Yerkes, R. M. & Dodson, J. D. The relation of strength of stimulus to rapidity of habit-formation. *J. Comp. Neurol. Psychol.* **18**, 459–482 (1908).
3. McGinley, M. J., David, S. V. & McCormick, D. A. Cortical membrane potential signature of optimal states for sensory signal detection. *Neuron* **87**, 179–192 (2015).
4. Hulsey, D., Zumwalt, K., Mazzucato, L., McCormick, D. A. & Jaramillo, S. Decision-making dynamics are predicted by arousal and uninstructed movements. *Cell Rep.* **43**, 113709 (2024).
5. Han, J. et al. Eyes-open and eyes-closed resting state network connectivity differences. *Brain Sci.* **13**, 122 (2023).
6. Agcaoglu, O., Wilson, T. W., Wang, Y.-P., Stephen, J. & Calhoun, V. D. Resting state connectivity differences in eyes open versus eyes closed conditions. *Hum. Brain Mapp.* **40**, 2488–2498 (2019).
7. Xu, P. et al. Different topological organization of human brain functional networks with eyes open versus eyes closed. *NeuroImage* **90**, 246–255 (2014).
8. Bianciardi, M. et al. Modulation of spontaneous fMRI activity in human visual cortex by behavioral state. *NeuroImage* **45**, 160–168 (2009).
9. Tagliazucchi, E. & van Someren, E. J. W. The large-scale functional connectivity correlates of consciousness and arousal during the healthy and pathological human sleep cycle. *NeuroImage* **160**, 55–72 (2017).
10. Tagliazucchi, E. & Laufs, H. Decoding wakefulness levels from typical fMRI resting-state data reveals reliable drifts between wakefulness and sleep. *Neuron* **82**, 695–708 (2014).
11. Tagliazucchi, E., Crossley, N., Bullmore, E. T. & Laufs, H. Deep sleep divides the cortex into opposite modes of anatomical–functional coupling. *Brain Struct. Funct.* **221**, 4221–4234 (2016).
12. Tong, C. et al. Multimodal analysis demonstrating the shaping of functional gradients in the marmoset brain. *Nat. Commun.* **13**, 1–15 (2022).
13. Liu, T. T. & Falahpour, M. Vigilance effects in resting-state fMRI. *Front. Neurosci.* **14**, 321 (2020).
14. Grimm, C. et al. Tonic and burst-like locus coeruleus stimulation distinctly shift network activity across the cortical hierarchy. *Nat. Neurosci.* **27**, 2167–2177 (2024).
15. Poe, G. R. et al. Locus coeruleus: a new look at the blue spot. *Nat. Rev. Neurosci.* **21**, 644–659 (2020).
16. Breton-Provencher, V. & Sur, M. Active control of arousal by a locus coeruleus GABAergic circuit. *Nat. Neurosci.* **22**, 218–228 (2019).
17. Kjaerby, C. et al. Memory-enhancing properties of sleep depend on the oscillatory amplitude of norepinephrine. *Nat. Neurosci.* **25**, 1059–1070 (2022).
18. Osorio-Forero, A. et al. Infraslow noradrenergic locus coeruleus activity fluctuations are gatekeepers of the NREM–REM sleep cycle. *Nat. Neurosci.* **28**, 84–96 (2025).
19. Howells, F. M., Stein, D. J. & Russell, V. A. Synergistic tonic and phasic activity of the locus coeruleus norepinephrine (LC-NE) arousal system is required for optimal attentional performance. *Metab. Brain Dis.* **27**, 267–274 (2012).

20. Zerbi, V. et al. Rapid reconfiguration of the functional connectome after chemogenetic locus coeruleus activation. *Neuron* **103**, 702–718.e5 (2019).
21. Oyarzabal, E. A. et al. Chemogenetic stimulation of tonic locus coeruleus activity strengthens the default mode network. *Sci. Adv.* **8**, eabm9898 (2022).
22. Lee, T.-H. et al. Arousal increases neural gain via the locus coeruleus–noradrenaline system in younger adults but not in older adults. *Nat. Hum. Behav.* **2**, 356–366 (2018).
23. Zou, Y. et al. Cell-type-specific optogenetic fMRI on basal forebrain reveals functional network basis of behavioral preference. *Neuron* **112**, 1342–1357.e6 (2024).
24. Yu, Y. et al. Sleep fMRI with simultaneous electrophysiology at 9.4 T in male mice. *Nat. Commun.* **14**, 1651 (2023).
25. Lindquist, M. A., Xu, Y., Nebel, M. B. & Caffo, B. S. Evaluating dynamic bivariate correlations in resting-state fMRI: a comparison study and a new approach. *NeuroImage* **101**, 531–546 (2014).
26. Gu, Y., Sainburg, L. E., Han, F. & Liu, X. Simultaneous EEG and functional MRI data during rest and sleep from humans. *Data Brief.* **48**, 109059 (2023).
27. Wong, C. W., Olafsson, V., Tal, O. & Liu, T. T. The amplitude of the resting-state fMRI global signal is related to EEG vigilance measures. *NeuroImage* **83**, 983–990 (2013).
28. Buchsbaum, M. S. et al. Regional cerebral glucose metabolic rate in human sleep assessed by positron emission tomography. *Life Sci.* **45**, 1349–1356 (1989).
29. Braun, A. R. et al. Regional cerebral blood flow throughout the sleep-wake cycle. An H215O PET study. *Brain* **120**, 1173–1197 (1997).
30. Song, C., Boly, M., Tagliazucchi, E., Laufs, H. & Tononi, G. fMRI spectral signatures of sleep. *Proc. Natl. Acad. Sci. USA* **119**, e2016732119 (2022).
31. Fei, Y. et al. Diverse and asymmetric patterns of single-neuron projectome in regulating interhemispheric connectivity. *Nat. Commun.* **15**, 3403 (2024).
32. van den Brink, R. L., Pfeffer, T. & Donner, T. H. Brainstem modulation of large-scale intrinsic cortical activity correlations. *Front. Hum. Neurosci.* **13**, 1–18 (2019).
33. Zerbi, V., Grandjean, J., Rudin, M. & Wenderoth, N. Mapping the mouse brain with rs-fMRI: an optimized pipeline for functional network identification. *NeuroImage* **123**, 11–21 (2015).
34. Feng, J. et al. A genetically encoded fluorescent sensor for rapid and specific in vivo detection of norepinephrine. *Neuron* **102**, 745–761.e8 (2019).
35. Feng, J. et al. Monitoring norepinephrine release in vivo using next-generation GRABNE sensors. *Neuron* **112**, 1930–1942.e6 (2024).
36. Lee, B. et al. Dopaminergic modulation and dosage effects on brain state dynamics and working memory component processes in Parkinson's disease. *Nat. Commun.* **16**, 2433 (2025).
37. Shine, J. M. et al. Human cognition involves the dynamic integration of neural activity and neuromodulatory systems. *Nat. Neurosci.* **22**, 289–296 (2019).
38. Munn, B. R., Müller, E. J., Wainstein, G. & Shine, J. M. The ascending arousal system shapes neural dynamics to mediate awareness of cognitive states. *Nat. Commun.* **12**, 1–9 (2021).
39. Durán, E., Yang, M., Neves, R., Logothetis, N. K. & Eschenko, O. Modulation of prefrontal cortex slow oscillations by phasic activation of the locus coeruleus. *Neuroscience* **453**, 268–279 (2021).
40. Vinck, M., Batista-Brito, R., Knoblich, U. & Cardin, J. A. Arousal and locomotion make distinct contributions to cortical activity patterns and visual encoding. *Neuron* **86**, 740–754 (2015).
41. Reimer, J. et al. Pupil fluctuations track rapid changes in adrenergic and cholinergic activity in cortex. *Nat. Commun.* **7**, 1–7 (2016).
42. Banerjee, S., Snyder, A. C., Molholm, S. & Foxe, J. J. Oscillatory alpha-band mechanisms and the deployment of spatial attention to anticipated auditory and visual target locations: supramodal or sensory-specific control mechanisms?. *J. Neurosci.* **31**, 9923–9932 (2011).
43. Goodale, S. E. et al. fMRI-based detection of alertness predicts behavioral response variability. *eLife* **10**, e62376 (2021).
44. Keller, A. S., Payne, L. & Sekuler, R. Characterizing the roles of alpha and theta oscillations in multisensory attention. *Neuropsychologia* **99**, 48–63 (2017).
45. Shine, J. M. et al. The dynamics of functional brain networks: integrated network states during cognitive task performance. *Neuron* **92**, 544–554 (2016).
46. Carro-Domínguez, M. et al. Pupil size reveals arousal level fluctuations in human sleep. *Nat. Commun.* **16**, 2070 (2025).
47. Liu, X. et al. Subcortical evidence for a contribution of arousal to fMRI studies of brain activity. *Nat. Commun.* **9**, 1–10 (2018).
48. Yang, Y., Leopold, D. A., Duyn, J. H., Sipe, G. O. & Liu, X. Sensory encoding alternates with hippocampal ripples across cycles of forebrain spiking cascades. *Adv. Sci.* **12**, 2406224 (2025).
49. Yang, Y., Leopold, D., Duyn, J. & Liu, X. Propagating cortical waves coordinate sensory encoding and memory retrieval in the human brain. Preprint at *bioRxiv* https://doi.org/10.1101/2024.06.24.600438 (2024).
50. Gu, Y. et al. Brain activity fluctuations propagate as waves traversing the cortical hierarchy. *Cereb. Cortex* **31**, 3986–4005 (2021).
51. Rodenkirch, C., Liu, Y., Schriver, B. J. & Wang, Q. Locus coeruleus activation enhances thalamic feature selectivity via norepinephrine regulation of intrathalamic circuit dynamics. *Nat. Neurosci.* **22**, 120–133 (2019).
52. Hofmeister, J. & Sterpenich, V. A role for the locus ceruleus in reward processing: encoding behavioral energy required for goal-directed actions. *J. Neurosci.* **35**, 10387–10389 (2015).
53. Bouret, S. & Richmond, B. J. Sensitivity of locus ceruleus neurons to reward value for goal-directed actions. *J. Neurosci.* **35**, 4005–4014 (2015).
54. Demirtaş, M. et al. Hierarchical heterogeneity across human cortex shapes large-scale neural dynamics. *Neuron* **101**, 1181–1194.e13 (2019).
55. Grandjean, J., Zerbi, X. V., Balsters, J. H., Wenderoth, X. N. & Rudin, M. Structural basis of large-scale functional connectivity in the mouse. *J Neurosci.* **37**, 8092–8101 (2017).
56. Gu, Y., Han, F. & Liu, X. Arousal contributions to resting-state fMRI connectivity and dynamics. *Front. Neurosci.* **13**, 1190 (2019).
57. Mateo, C., Knutsen, P. M., Tsai, P. S., Shih, A. Y. & Kleinfeld, D. Entrainment of arteriole vasomotor fluctuations by neural activity is a basis of blood-oxygenation-level-dependent "resting-state" connectivity. *Neuron* **96**, 936–948.e3 (2017).
58. Suárez, L. E., Markello, R. D., Betzel, R. F. & Misic, B. Linking structure and function in macroscale brain networks. *Trends Cogn. Sci.* **24**, 302–315 (2020).
59. Musall, S., Kaufman, M. T., Juavinett, A. L., Gluf, S. & Churchland, A. K. Single-trial neural dynamics are dominated by richly varied movements. *Nat. Neurosci.* **22**, 1677–1686 (2019).
60. Allen, P. J., Josephs, O. & Turner, R. A method for removing imaging artifact from continuous EEG recorded during functional MRI. *NeuroImage* **12**, 230–239 (2000).
61. Tong, C. et al. Differential coupling between subcortical calcium and BOLD signals during evoked and resting state through simultaneous calcium fiber photometry and fMRI. *NeuroImage* **200**, 405–413 (2019).
62. Kim, C. K. et al. Simultaneous fast measurement of circuit dynamics at multiple sites across the mammalian brain. *Nat. Methods* **13**, 325–328 (2016).
63. Chen, X. et al. Sensory evoked fMRI paradigms in awake mice. *NeuroImage* **204**, 116242 (2020).
64. Schaefer, A. et al. Local-global parcellation of the human cerebral cortex from intrinsic functional connectivity MRI. *Cereb. Cortex* **28**, 3095–3114 (2018).

65. Tian, Y., Margulies, D. S., Breakspear, M. & Zalesky, A. Topographic organization of the human subcortex unveiled with functional connectivity gradients. *Nat. Neurosci.* **23**, 1421–1432 (2020).
66. Diedrichsen, J., Balsters, J. H., Flavell, J., Cussans, E. & Ramnani, N. A probabilistic MR atlas of the human cerebellum. *NeuroImage* **46**, 39–46 (2009).
67. Bianciardi, M. et al. Toward an in vivo neuroimaging template of human brainstem nuclei of the ascending arousal, autonomic, and motor systems. *Brain Connect* **5**, 597–607 (2015).
68. Coletta, L. et al. Network structure of the mouse brain connectome with voxel resolution. *Sci. Adv.* **6**, eabb7187 (2020).
69. Markello, R. D. & Misic, B. Comparing spatial null models for brain maps. *NeuroImage* **236**, 118052 (2021).

## Acknowledgements

The authors thank Xiao Liu (The Pennsylvania State University, University Park, PA, USA), Mara Mather (University of Southern California, Los Angeles, CA, USA), Cirong Liu (Center for Excellence in Brain Science and Intelligence Technology, CAS, China) and Valerio Zerbi (ETH Zürich, Zürich, Switzerland) for their kind sharing of neuroimaging datasets. Authors also thank Mouse Facility of Center for Excellence in Brain Science and Intelligence Technology (Institute of Neuroscience) for animal care, and Brain Science Data Center, Chinese Academy of Sciences for dataset release. This work was supported by the National Science and Technology Innovation 2030 Major Program (2021ZD0202200 and 2021ZD0200100 to Z.L.), National Natural Science Foundation of China (82402245 to C.T., 82171899 to Z.L. and Excellent Young Scientists Fund 32322036 to Z.L.), Shanghai Municipal Science and Technology Major Project (2019SHZDZX02 to Z.L.), China National Postdoctoral Program for Innovative Talents (BX20230383 to C.T.), China Postdoctoral Science Foundation (2023M743616 to C.T.), Shanghai Post-doctoral Excellence Program (2023759 to C.T.) and Special Research Assistant Project of the Chinese Academy of Sciences (C.T.).

## Author contributions

C.T. and Z.L. designed and supervised the study; C.T., W.L., Y.Z., Y.X., M.P., K.Z. and Y.L. collected the multimodal fMRI data; C.T., W.L., Y.Z., and Z.L. carried out the analysis and organized the results; C.T. and Z.L. wrote the original draft and revised the draft.

## Competing interests

The authors declare no competing interests.

## Additional information

**Supplementary information** The online version contains supplementary material available at https://doi.org/10.1038/s41467-025-66436-x.

**Correspondence** and requests for materials should be addressed to Chuanjun Tong or Zhifeng Liang.

**Peer review information** *Nature Communications* thanks Yen-Yu Shih, who co-reviewed with Li-Ming Hsumand Xiao Liu and Valerio Zerbi for their contribution to the peer review of this work. A peer review file is available.